[†]Deceased.

Key Points:
- NRM of the EGMA exhibits a component of inverse polarity coherent with the characteristics of the Kiaman superchron
- Synkinematic S-Type granitoids of the Lugo-Sanabria dome are heterogeneously but highly magnetic
- Late Variscan extension produced the magnetization of EGMA and other areas at the core of the Central Iberian Arc during the Kiaman superchron

Correspondence to:

P. Ayarza,
puy@usal.es

Characterizing the Source of the Eastern Galicia Magnetic Anomaly (NW Spain): The Role of Extension in the Origin of Magnetization at the Central Iberian Arc

Puy Ayarza[1], Juan José Villalaín[2], José Ramón Martínez Catalán[1], Fernando Álvarez Lobato[1,†], Manuela Durán Oreja[1], Pablo Calvín[2], Clemente Recio[1], Mercedes Suárez Barrios[1], and Elena Gómez Martín[1]

[1]Departamento de Geología, Universidad de Salamanca, Salamanca, Spain, [2]Departamento de Física, Universidad de Burgos, Burgos, Spain

Abstract The Eastern Galicia Magnetic Anomaly is the best studied anomaly of the Central Iberian Arc. This is due to its location, on the Lugo-Sanabria gneiss dome, and to the fact that its source rocks crop out in the Xistral Tectonic Window. Multiple studies of this anomaly have been carried out, but still, new results keep on shedding light on its understanding. This paper presents the first results on rock magnetic analyses, natural remanent magnetization, anisotropy of the magnetic susceptibility, X-ray diffraction, and stable isotopes geochemistry carried out on the source rocks of this anomaly. Results suggest that magnetization responds to the increase in oxygen fugacity underwent by rocks affected by late Variscan (330-300 Ma) extensional tectonics. Extensional detachments were the pathways that allowed the entrance of fluids that led to syntectonic crystallization of magnetite and hematite in metasediments and inhomogeneous S-Type granitoids derived from their partial melting. Accordingly, magnetization is not linked to lithologies, but to extensional structures developed in the late Carboniferous/earliest Permian, during the Kiaman reverse superchron. Systematic reverse magnetic remanence exhibited by hematite-bearing samples confirms the age of the magnetization and adds complexity to the interpretation of the anomaly. Understanding the EGMA contributes to the interpretation of other anomalies existing in the CIA, also located on thermal domes. The observed extension-related magnetization probably affected most of the NW Iberian Massif, thus hindering the study of previous tectonics by paleomagnetic techniques. This work aims to provide new hints to interpret magnetic anomalies located in extensional tectonic contexts worldwide.

Plain Language Summary This paper presents a further step in the understanding of the Eastern Galicia Magnetic Anomaly (Iberian Massif), the biggest and most studied magnetic anomaly in Spain. Understanding the source and age of magnetization of this anomaly is key to understand the age of the Central Iberian Arc as it allows (1) to infer the origin of other anomalies found in the internal zone of the Central Iberian Arc and (2) shed more light on the age of the arc itself. Previous papers on this matter are: Ayarza et al. (2007) and Martínez Catalán et al. (2018), https://doi.org/10.1029/2017tc004887. Both represent the evolution on the investigations carried out in this area after the papers by Aller et al. (1994), https://doi.org/10.1016/0040-1951(94)90255-0 and that of de Poulpiquet (2012). The MS submitted now includes new AMS, rock magnetism, NRM, field work, and geochemistry studies of the area and proves the role that late Variscan orogenic extension has played in magnetization.

1. Introduction

Aeromagnetic data are a valuable source of geological information. Regional datasets have been commonly used to (1) establish the depth to the Curie Point and hence the thermal structure of large areas (Andres et al., 2018; Lawal & Nwankwo, 2017; Salem et al., 2014), (2) to unravel the basement structure and depth (Ali et al., 2017; Baptiste et al., 2016; Bascou et al., 2013), (3) to map mineral deposits (Dufréchou et al., 2015) and fractures (Grauch et al., 2001), (iv) to establish relationships with certain types of mineralizations (Sant'Ovaia et al., 2013, pp. 33–39), (v) to contribute to the knowledge of crustal structure and evolution (Calvín et al., 2014; Pedreira et al., 2007), etc. As a rule of thumb, the minimum wavelength of aeromagnetic anomalies coincides with the altitude of acquisition. Thus, large regional-scale maps usually

lack the resolution to carry out detailed interpretations of the source of the anomaly. Furthermore, the diagnostic potential of these datasets decreases if the source of the magnetic anomaly is not identified. In these cases, resulting models are a trade-off between the unknown magnetic susceptibility and magnetic remanence, and the size and depth of magnetic bodies, leading to multiple and poorly constrained solutions.

The aeromagnetic map of the Iberian Peninsula (Figure 1, Socias & Mezcua, 2002) is based on datasets acquired in 1986–1987 in Spain (Ardizone et al., 1989) and between 1979 and 1981 in Portugal (Miranda et al., 1989). It features a number of high amplitude anomalies that, in the western part of Iberia, present also long wavelengths partly resulting from the altitude of acquisition (3,000 m), but also indicative of the presence of deep sources. These anomalies often coincide with Variscan thermal domes, i.e., prominent structures where high-grade metamorphic rocks and granitoids occur at relatively high crustal levels. Thus, the latter may be key features in the interpretation of the anomalies and in understanding the tectonic evolution of the Iberian Massif.

One of such features is the Eastern Galicia Magnetic Anomaly (EGMA; Aller et al., 1994). This anomaly coincides with the Lugo-Sanabria Dome, a late Variscan (330-300 Ma) extensional structure that straddles the boundary between the West Asturian-Leonese Zone and Central Iberian Zone (Figure 1). In the N, both zones are separated by an important extensional feature, the W-dipping, normal Viveiro Fault, which shows high offsets that put into contact Precambrian rocks to the E with Silurian and Ordovician metasediments and metavolcanics to the W. The EGMA is also one of the most conspicuous anomalies of the Central Iberian Arc (CIA), an orocline that has been partly defined by the curvature of the magnetic anomalies in its external part (Aerden, 2004; Martínez Catalán, 2011, 2012). However, the most important anomalies occur at the core of the arc (Figure 1b): the EGMA, the Tormes Dome Magnetic Anomaly (TDMA), the Central System Magnetic Anomaly (CSMA), and its prolongation to Porto in Portugal along the Porto-Viseu-Guarda Magnetic Anomaly (PVGMA).

Interpretations of the EGMA have somehow followed the evolution of the understanding of the Lugo-Sanabria Dome. Primarily this structure was viewed as an antiformal stack resulting from the first stages of Variscan compression (Pérez-Estaún et al., 1991) Accordingly, Aller et al. (1994) explained the EGMA as the result of the emplacement of dense basic and ultrabasic rocks at high crustal levels due to Variscan thrusting. However, this interpretation lacked the constraints provided by outcropping magnetic rocks, and failed to explain the low Bouguer gravity anomaly of the area. Later on, the reinterpretation of the Lugo-Sanabria Dome in the light of evidences of extensional tectonics (Arenas & Martínez Catalán, 2003; Martínez Catalán et al., 2003) led to models were the EGMA resulted from magnetite-rich migmatites and heterogeneous granites outcropping in the Xistral Tectonic Window, at the core of the Lugo Dome, and formed during the late Variscan extensional event (Ayarza & Martínez Catalán, 2007). These models were backed up by ca. 1,000 in situ measurements of magnetic susceptibility of rocks and by its gravity response, which fitted the observed Bouguer gravity anomaly. Later models (de Poulpiquet, 2012) considered the EGMA as a result of mixed sources, with a shallow contribution of granitic composition and a deeper mafic one that controlled its long wavelength. Lastly, high-resolution magnetic mapping of the EGMA in its northern part, the Xistral Tectonic Window, has led to models where extensional detachments affecting metasediments, migmatites, and inhomogeneous granites are the key to magnetization (Martínez Catalán et al., 2018).

Regardless of the number of interpretations, the EGMA and the rest of the magnetic anomalies defining the CIA are not fully understood. Despite these anomalies being geographically related with thermal domes, magnetic rocks have only been identified in the northern part of the EGMA, where the Xistral Tectonic Window allows access to deep parts of the crust, thus providing insights to the geometry and effects of extensional structures. But even in this case, magnetic remanence has been undersampled as lithologies with high Königsberger ratios (Qn) where initially ignored. In this area, Anisotropy of the Magnetic Susceptibility (AMS) studies have been only devoted to nonmagnetic, synorogenic, and late-orogenic granites and have been mostly related to intrusion patterns (Aranguren et al, 1991, 2003; Aranguren & Tubia, 1994). Finally, no detailed rock magnetic analyses exist for any of the CIA anomalies.

In this paper, we present a detailed analysis of the magnetic properties of the rocks that, according to Ayarza and Martínez Catalán (2007) and Martínez Catalán et al. (2018) are the source of the EGMA. These rocks are characterized by, at least, two diachronous populations of magnetic minerals that exhibit high magnetic
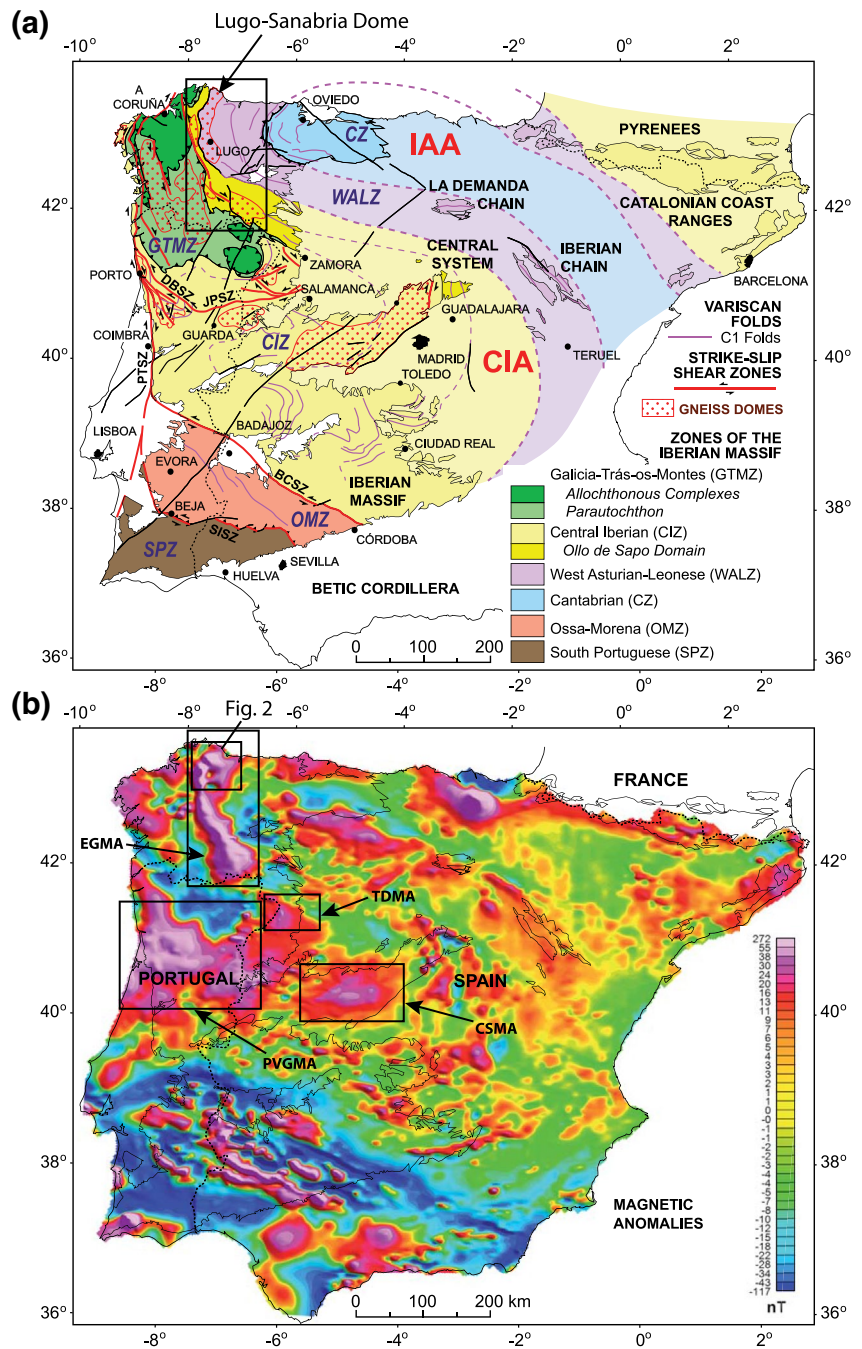
Figure 1. (a) Map of the the Iberian Massif showing its zonation and the location of the EGMA. IAA: Ibero-Armorican Arc. CIA: Central Iberian Arc. The rectangle delimits the area of the Lugo-Sanabria Dome. (b) Aeromagnetic map of the Iberian Peninsula (data from Ardizone et al., 1989; Miranda et al., 1989; Socias & Mezcua, 2002). Rectangles define the main magnetic anomalies of the CIA, namely EGMA, Eastern Galicia Magnetic Anomaly; TDMA, Tormes Dome Magnetic Anomaly; CSMA, Central System Magnetic Anomaly; PVGMA, Porto-Viseu-Guarda Magnetic Anomaly.

susceptibilities and intense magnetic remanence, a very high AMS factor, and high $\delta^{18}O$ ratios. These characteristics further help to understand the origin of the EGMA and set the basis for the next generation of models. Also, this paper briefly analyzes the rest of the anomalies of the CIA, providing a hypothesis for the lack of magnetic outcrops and the mechanisms that may have led to magnetization. Finally, we emphasize the complexity inherent to the interpretation of magnetic anomalies. Often, they are not thoroughly

investigated, and studies that allowed to relate them with known outcropping lithologies and structures are missing.

2. Geological and Geophysical Setting

The Central Iberian Arc (CIA, Figure 1) is an oroclinal structure located in the central part of Iberia. It was defined on the basis of the geometry of Variscan folds and by its curved and conspicuous magnetic signature (Martínez Catalán, 2011, 2012; Martínez Catalán et al., 2015). It is contiguous to the Ibero-Armorican Arc and has an opposite curvature. Both arcs are not coeval, and structural crosscutting relationships show that the Central Iberian Arc is older (Martínez Catalán, 2012). The CIA is mainly developed in the Central Iberian Zone (CIZ), although its core is occupied by the Galicia-Trás-Os-Montes Zone (GTMZ) the most internal part of the Iberian Variscides. The latter is characterized by a stack of allochthonous terranes preserved as a klippen (Figure 1a), and represent the suture of a Variscan (Devono-Carboniferous) collision. The existence of the CIA has been the key to understand the anomalous width of the CIZ and has opened the debate to new interpretations on the evolution of the European Variscides. For an historical review see Martínez Catalán et al. (2015).

The study area, the Lugo-Sanabria Dome, lies in the boundary between the West Asturian-Leonese Zone (WALZ) and the Central Iberian Zone (CIZ) of the Iberian Massif, which represents the largest outcrop of the Variscan basement in the Iberian Peninsula (Figure 1a). The tectonic evolution of these two internal zones is characterized by three compressional phases (C1, C2, and C3) and two extensional stages (E1 and E2). Although these tectonic episodes partly overlap, they are diachronous and a deformation sequence can be established (Alcock et al., 2015; Dallmeyer et al., 1997; Martínez Catalán et al., 2014): C1 (360-335 Ma) is the response to the initial plate convergence and is characterized by E-vergent recumbent folds and S1 schistosity. The progression of the collision developed a second compressional phase, C2 (345-320 Ma), characterized by reverse ductile shear zones and thrust faults that cut and displace the C1 folds. A second mylonitic schistosity, S2, accompanies this deformation. The main structure of this phase is the Mondoñedo Nappe basal thrust (Figure 2c). Crustal thickening due to shortening triggered heating, and after several million years of thermal relaxation, gravitational collapse produced the first extensional episode, E1 (330-315 Ma). Gneiss domes started to form together with normal faults, conjugated E-dipping and W-dipping extensional detachments and SE1 schistosity. Then, oblique plate convergence occurred with a strong component of dextral transcurrence, resulting in a C3 deformation phase (315-305 Ma) of strike-slip ductile shear zones and associated upright folds with an axial planar S3 crenulation or slate cleavage (Díez Fernández & Pereira, 2017; Gutiérrez-Alonso et al., 2015; Iglesias Ponce de León & Choukroune, 1980). Crustal thickening continued in the external Cantabrian Zone (CZ) between 325 and 300 Ma while the internal zones had not been fully re-equilibrated (Merino-Tomé et al., 2009; Pérez-Estaún et al., 1991). This resulted in a second extensional event, E2 (310-295 Ma), which locally developed a SE2 foliation. New extensional detachments and gneiss domes formed. Among them, the Viveiro normal extensional detachment and fault and the Lugo-Sanabria Dome are some of the most important features (Figure 2). The extensional tectonics episodes also triggered the formation and emplacement of a wide range of granites in other areas of the CIZ like northern Portugal, the Tormes Dome, and the Central System. Finally, late Variscan NW-SE and NE-SW faulting puts an end to the Variscan deformation in the internal Iberian Massif. Alpine tectonics played an important role in reactivating Variscan faults in the Central System (de Vicente et al., 1996; Vegas et al., 1990), but its effect was limited in the rest of the CIZ.

Accompanying these deformation phases, three metamorphic events are identified (Arenas & Martínez Catalán, 2003): M1 is a regional Barrovian event characterized by the development of chlorite, biotite, garnet, staurolite, and kyanite during C1 and C2. M2 is a high temperature/low pressure (HT/LP) event that represents the thermal peak reached after C2 and heralding E1 and later extension. During M2, sillimanite-orthoclase conditions were met, resulting in widespread migmatization and crustal melting. This metamorphism was contemporaneous with E1, C3, and E2. M3 represents a retrograde metamorphism associated with late stages of C2, E1, and E2 structures as well as with C3 ductile shearing.

The stratigraphic sequence of the WALZ spans from the Neoproterozoic terrigenous Vilalba Series to Lower Devonian metasediments. The Vilalba series is composed of more than 3,000 m of slates and metagreywackes
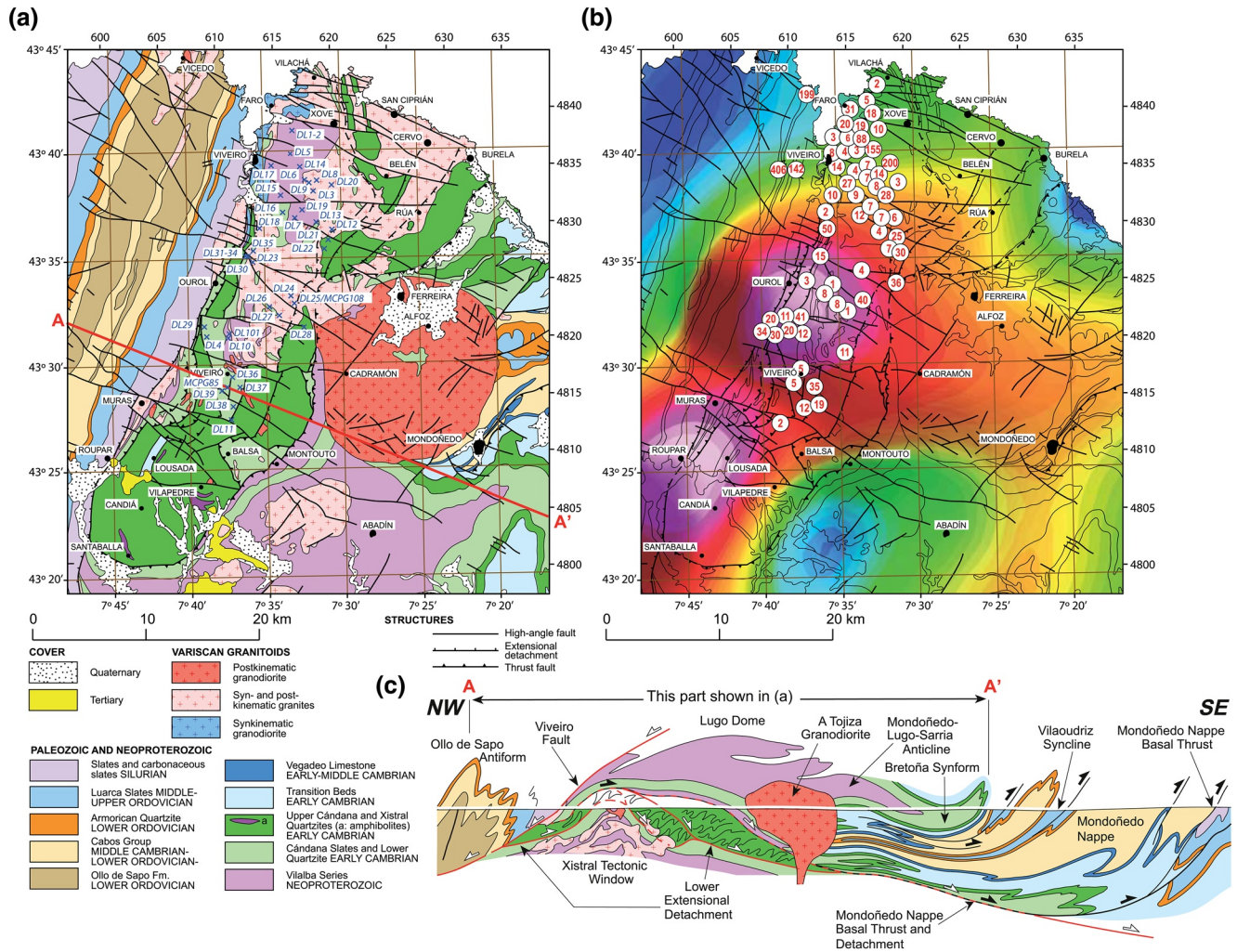
Figure 2. (a) Geological map of the Xistral Tectonic Window with the location of the samples used for this study (same color code as in Figure 1). (b) Aeromagnetic map of the EGMA with the magnetic susceptibilities measured in the field ($10^3 \times$ (SI)). (c) Cross section A-A′ of Figure 2a continued to the SE to show the whole structure of the Mondoñedo Nappe. EGMA, Eastern Galicia Magnetic Anomaly.

which evolved to paragneisses, migmatites, and inhomogeneous granites in the autochthon of the Mondoñedo Nappe cropping out in the Xistral Tectonic Window (Figure 2a). Unconformably above them, the Paleozoic features up to 8,000 m of platform facies slates, sandstones and carbonates ranging from the early Cambrian to the Lower Devonian without significant discontinuities. In the adjacent CIZ to the W, the sequence is similar but includes an important event of Lower Ordovician felsic volcanism, the Ollo de Sapo Fm. (Díez Montes et al., 2010; Parga Pondal et al., 1964).

The Lugo-Sanabria Dome is a N-S antiformal structure, slightly concave to the E, developed essentially during the E2 event. Previously, the basal thrust of the Mondoñedo Nappe was reactivated as, or cut across by an extensional structure, and at least an important extensional detachment developed in the relative autochthon: the Lower Extensional Detachment (Figure 2c). These structures can be studied in the Xistral Tectonic Window. They were formed prior to doming and might be attributed to E1, while the Viveiro Fault and associated 2–3 km wide shear zone is coeval with, and contributed to the dome development during E2. The age of the early extensional deformation (E1) is constrained at ca. 313 Ma by deformation of a synkinematic granite (Fernández-Suárez et al., 2000). The dome and the Viveiro Fault overprints deformation in this and other somewhat older granitoids, and are not precisely dated. However, Ar-Ar ages around 300 Ma in schists of the Lugo Dome probably reflect resetting or cooling, and are a reference for the age of the dome (Dallmeyer et al., 1997).

Detachments developed during E1 and E2 eased the intrusion of partial melts and probably the circulation of various fluids. The Viveiro Fault continues another 90 km to the S of the Xistral Tectonic Window bounding the western limb of the Lugo Dome. Then it is replaced by the Chandoiro Fault, which features an equivalent structural relationship with the Sanabria Dome (Díez Montes et al., 2010). No magnetic rocks have been found to the S of the Xistral Tectonic Window, but the continuation of the EGMA there suggests that the early detachments and magnetic rocks continue at depth to the S (Martínez Catalán et al., 2018).

The EGMA overlaps the Lugo-Sanabria Dome (Figure 2b). This anomaly is the largest in size and the second in amplitude in Spain. It reaches maxima of 190 nT in the aeromagetic dataset (Ardizone et al., 1989) and a total amplitude of ~1,100 nT in the ground-based dataset (Martínez Catalán et al., 2018). This anomaly was first described and studied by Aller et al. (1994). These authors interpreted it as the result of a middle-lower crustal body of highly magnetic mafic or ultramafic rocks emplaced by the so-called eastern Galicia thrust at upper crustal levels. In addition, the northernmost part of the anomaly was attributed to ultramafic rocks intruded during the Variscan orogeny cropping out near the Viveiro Fault. This model was supported by the existence of high velocity rocks modeled from wide angle seismic reflection and refraction data (Córdoba et al., 1987) in the Lugo Dome. However, it failed to explain the gravity signature in the area, which is characterized by lower values in the Lugo Dome and higher values to the W of the Viveiro Fault (Ayarza & Martínez Catalán, 2007).

This model was later revisited considering the interpretation of the Lugo Dome as an extensional dome instead of an antiformal stack (Martínez Catalán et al., 2003). The identification of highly magnetic migmatites and inhomogeneous granites in the Xistral Tectonic Window (Ayarza & Martínez Catalán, 2007) opened the door to a new model where a lens-shaped body of felsic rocks was the source of the anomaly. Although this body cropped out in the above-mentioned tectonic window, in the northern part of the Lugo Dome, it was interpreted to reach midcrustal depths. The magnetic susceptibility attributed to these rocks reached $\kappa = 0.03$ (SI), and was in accordance with measured in situ values. The main identified magnetic mineral was multidomain (MD) magnetite (size up to 1 cm) but alterations of the latter to hematite where also reported. However, this model also failed to include the effect of possible magnetic remanence which would have changed the geometry and depth of magnetic bodies, did not provide an explanation for the origin of the observed heterogeneous magnetization and excluded anisotropy studies that could relate the anomaly with structures (Ayarza & Martínez Catalán, 2007).

A further step to understand the EGMA suggested that the magnetic anomaly of the South Armorican continental shelf is the continuation of the EGMA (de Poulpiquet, 2012), thus resulting in a 600 km long arcuate feature that is interpreted as the magnetic signature of the relics of a Cambro-Ordovician aborted rift. Again, the source of magnetism is primarily addressed to deep mafic rocks, although the anomaly needs the contribution of a shallower source that could correspond to the migmatites and inhomogeneous granites modeled by Ayarza and Martínez Catalán (2007). As in previous models, a detailed characterization of the source of the anomaly is missing and thus, the interpretation relies merely on the fit of the observed and modeled anomalies, without considerations about origin, age, and remanence of the magnetization.

Finally, the acquisition of detailed ground-based magnetic data has allowed to present the most detailed interpretation of the EGMA up to date (Martínez Catalán et al., 2018). These authors show that, when looked in detail, the EGMA magnetic maxima overlap extensional features, most importantly the Viveiro Fault extensional detachment. Their resulting models include preliminary results of magnetic remanence and their final interpretation indicates that the magnetization is not linked to a particular lithology but to extensional tectonics features.

No regional magnetic studies have been presented as yet of the TDMA, CSMA, and PVGMA. Although some paleomagnetic data exist (e.g., Palencia Ortas et al., 2006; Pastor-Galán et al., 2016) no inferences to the origin of the anomalies have been done. However, studies of the characteristics of the rocks that underlie them indicate that, for the CSMA and the PVGMA, they are mostly granites belonging to the I-Type, although there are also S-Type granites (e.g., Sant′Ovaia et al., 2013; Villaseca et al., 2017). But most importantly, these studies indicate that these granites are, very seldom, magnetic. Only the Lavadores granite to the S of Porto and La Pedriza Batholith in the Central System show moderate to high magnetic susceptibilities ($\kappa = 0.001-0.04$ (SI)) that, even though may result in local magnetic anomalies, cannot explain the maxima observed in the PVGMA and the CSMA, respectively.

3. Characterization of the EGMA

During the last decade, several studies have been carried out at the Xistral Tectonic Window, where outcropping magnetic lithologies have been found and are thought to be the source of the EGMA. Detailed surveying has included the acquisition of ground-based magnetic data and collection of samples for characterization studies. The map resulting from land acquisition (Martínez Catalán et al., 2018) is shown in Figure 3, with the location and number of paleomagnetic sites in color coded labels according to their Königsberger ratios (Qn). Thorough tracking of the anomaly and later mapping showed that not only late Carboniferous migmatites and inhomogeneous granites where highly magnetic (Ayarza & Martínez Catalán, 2007), but Neoproterozoic and early Cambrian metasediments (quartzites, schists, and gneisses) were also found to be magnetic in some areas (Figures 4c and 4d). In fact, the latter sometimes appeared as enclaves in late, non-magnetic granites (Figures 4a and 4b), raising the question about the origin of the magnetization.

According to the above, samples from 39 locations were picked (Figure 3). These include metasediments, inhomogeneous syntectonic granites, migmatites, and late undeformed granites. A variable number of cores (between 4 and 10 depending on the degree of alteration and size of the outcrop) were taken at each site using a portable gas drill. Multiple studies were carried out in these samples in order to characterize their magnetic properties, including the natural remanent magnetization (NRM). The next sections include a description of the methods applied and their results.

3.1. Optical and Microprobe (MP) Identification of Minerals

The magnetic behavior of a rock is strongly controlled by its mineral content. The existence of minerals belonging to the titanomagnetite and titanohematite series is most commonly responsible of rock's magnetic properties. Magnetic samples of the Xistral Tectonic Window have been studied by optical microscopy. Conflicting identifications were aided by additional studies undertaken by a JEOL-Superprobe JXA-8900M microprobe with five spectrometers from the ICTS-National Electronic Microscope Center (https://www.cnme.es) at Complutense University of Madrid (Spain).

In the studied samples, magnetite and hematite are the most common magnetic minerals. In granites and migmatites, magnetite often presents exsolutions of ilmenite (Figures 5a and 5c) and, in some cases it is also altered to hematite (Figures 5b and 5c). Transformation of biotite to magnetite has also been observed (Figure 5d). Finally, unaltered hematite (Figure 5f), sometimes presenting exsolutions with rutile (Figure 5e), is found in samples with low magnetic susceptibility. These crystals have no apparent relation with magnetite. Grain size goes from a couple of cm, clearly identifiable at outcrop scale (e.g., in DL8, Figure 3), to μm. Grain shape varies from equigranular to elongated and subparallel to the stretching lineation.

3.2. Rock Magnetic Analyses

Different rock magnetic experiments have been carried out in the Paleomagnetic Laboratory of Universidad de Burgos in order to determinate the main ferromagnetic s.l. minerals. Isothermal remanent magnetization (IRM) acquisition and backfield curves, hysteresis loops as well as induced magnetization thermomagnetic curves have been measured by means of a variable field translation balance (MMVFTB, Magnetic Measurements).

The behavior of samples can be classified in between two end-members that we will describe as Type A and Type B (Figure 6). The Type A group of samples shows the contribution of only low or even medium coercivity minerals to the IRM, being saturated at fields lower than 300 mT (Figures 6a–6c). Their thermomagnetic curves present almost reversible cycles showing very sharp decays at about 575°C characteristic of the Curie temperature of Ti-free magnetite (Figures 6g–6i). Type B samples present a more complicated magnetic mineralogy. Its IRM acquisition pattern shows an inflexion at about 200 mT due to the saturation of a low coercivity phase (Figures 6d–6f). However, this phase coexists with others that are not saturated at the maximum applied field of 1 T. The induced magnetization thermomagnetic curves of this group show also sharp Curie points at temperatures typical of magnetite. Nevertheless, they also present falls at higher temperatures (above 600 °C), probably caused by low-Ti content titanohematite (Figures 6j–6l). Hysteresis loops of Type A samples present narrow patterns with only one magnetic phase and very low coercivity of
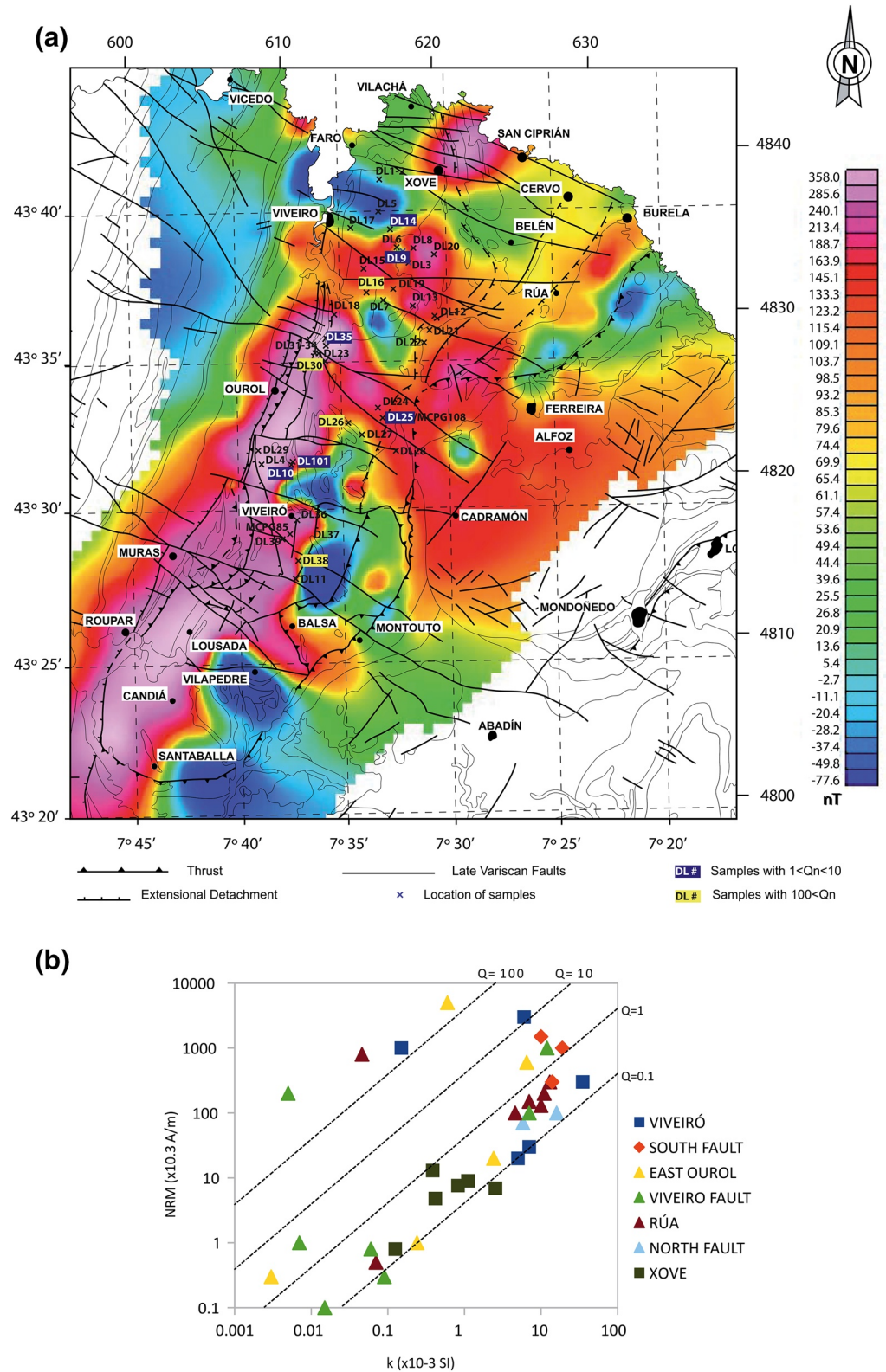
Figure 3. (a) High-resolution magnetic map of the Xistral Tectonic Window. The location of the magnetic samples is also shown. Color coded labels indicate sites where Qn > 1. Observe how most of the latter samples lie to the NW of a pronounced minimum, thus indicating their influence in the anomaly (modified from Martínez Catalán et al., 2018). (b) Classification of samples according to their Qn. Groups with their precise Qn values are described in Table 1.
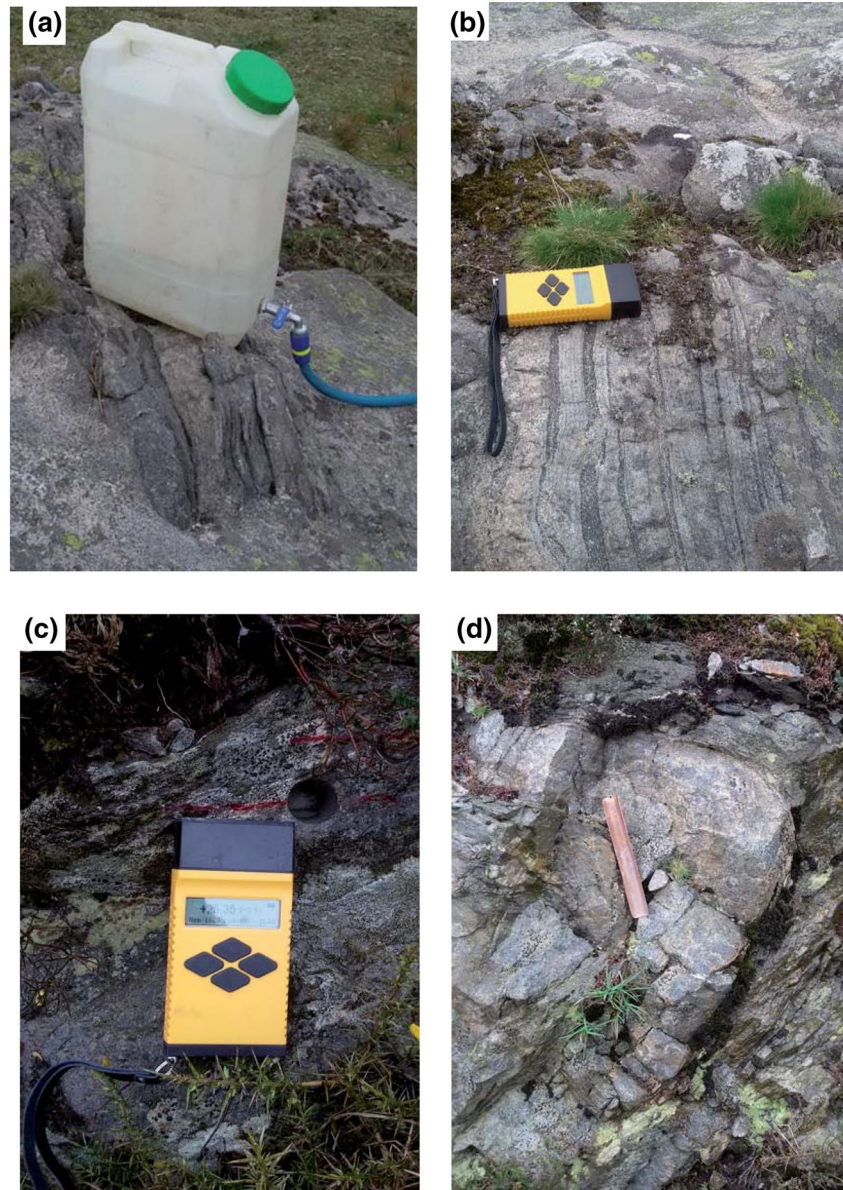
Figure 4. Outcropping magnetic metasediments. (a) and (b) Enclaves of alternating schists and quartzites with high magnetic susceptibility in postkinematic, nonmagnetic granites. (c) Magnetic schist. (d) Folded magnetic quartzite. All samples are located at or near site DL25/MCPG108.

less than 3 mT, characteristic of multidomain (MD) magnetite (Figures 6m–6o). However, Type B samples show wasp-waisted shape curves characteristic of rocks where different coercivity fractions coexist (Figures 6p–6r). Following the interpretation of the experiments described above, A-Type samples may represent MD magnetite whereas B-Type samples also show the presence of magnetite but with a contribution of hematite. Type A samples do not show any contribution of paramagnetic minerals, but Type B samples do. This might be due to the higher induced magnetization of Type A samples masking the presence of paramagnetic minerals, although different metamorphic evolutions for both types of samples cannot be ruled out.

Susceptibility thermomagnetic curves have also been obtained by means of a KLY4S Kappabridge (AGI-CO) susceptometer with a CSL cryostat ($-195\ °C < T^a < 0\ °C$) and a CS3 furnace ($710\ °C > T^a > 25\ °C$). Figure 7 shows two of these examples obtained in B-Type samples. The low-temperature heating presents
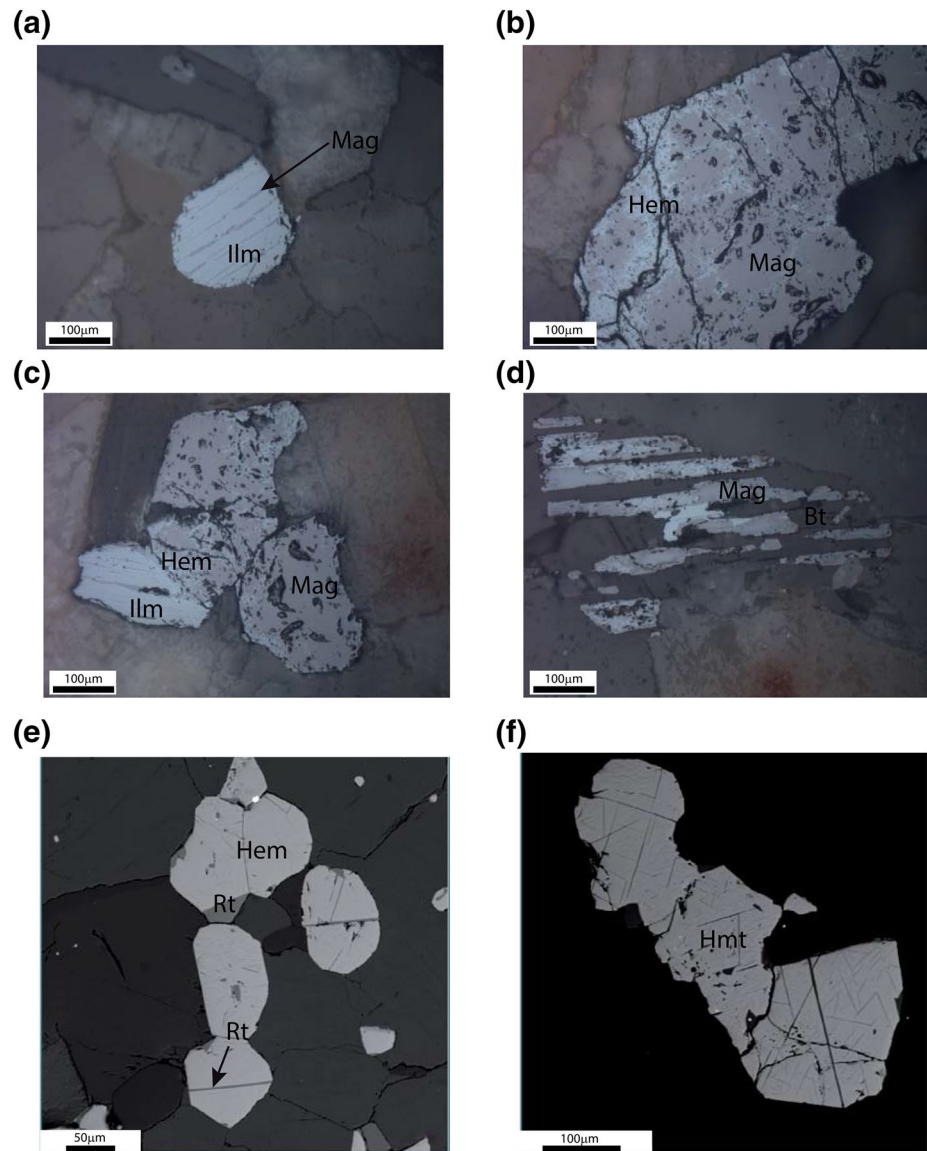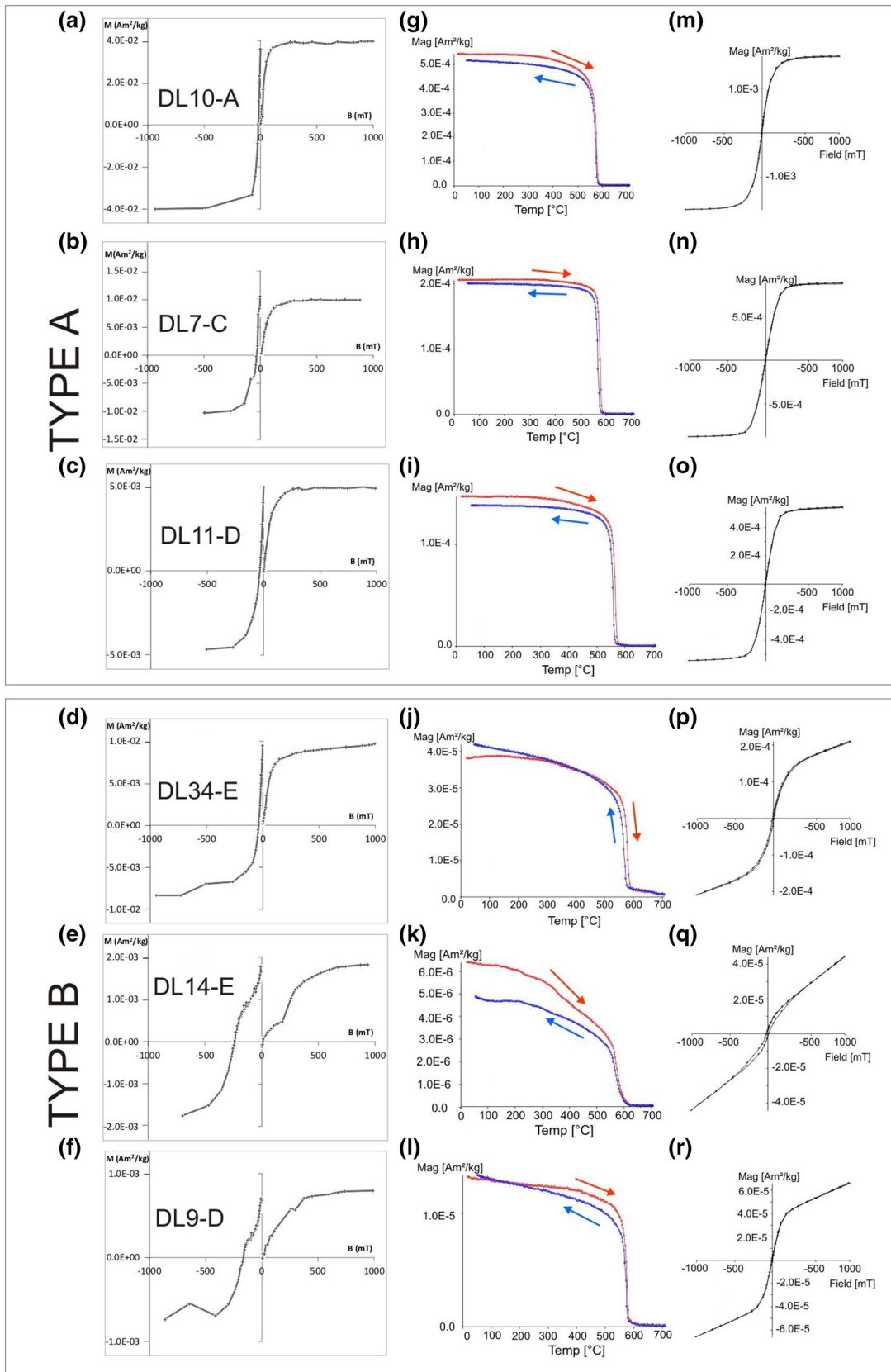
Figure 5. Optical microscope and microprobe images of magnetic minerals. (a) Magnetite with exsolved ilmenite. (b) Magnetite altered to hematite. (c) Magnetite with exsolved ilmenite and magnetite altered to hematite. (d) Alteration of biotite to magnetite. (e) Hematite with exolved rutile. (f) Pure hematite.

a clear Verwey transition at −160 °C characteristic of pure magnetite (Verwey, 1939; Walz, 2002). The high temperature cycles are roughly reversible and define a pronounced decay of susceptibility around 580 °C confirming the dominance of magnetite. Another smoothed step can be observed at around 620 °C that could be caused by low-Ti content titanohematite, as it has been showed in the magnetization thermomagnetic experiments. This experiment also indicates that the susceptibility is dominated by the ferromagnetic fraction since the hyperbolic decrease typical of paramagnetic minerals cannot be observed.

Figure 8 shows the Day plot (Day et al., 1977; Dunlop, 2002) for A-Type and B-Type samples together with the theoretical curves (Dunlop, 2002) for SD-MD and SP-SD magnetite mixtures. Type A samples are clustered into the MD area whereas the rest (B-Type samples) show a heterogeneous distribution that can be related with the more complex magnetic mineralogy (presence of magnetite and hematite) rather than the grainsize of the former, since these curves are defined only for Ti-free magnetite (Dunlop, 2002). In fact, the samples with highest content of hematite as DL14 show outsider's points in the diagram.
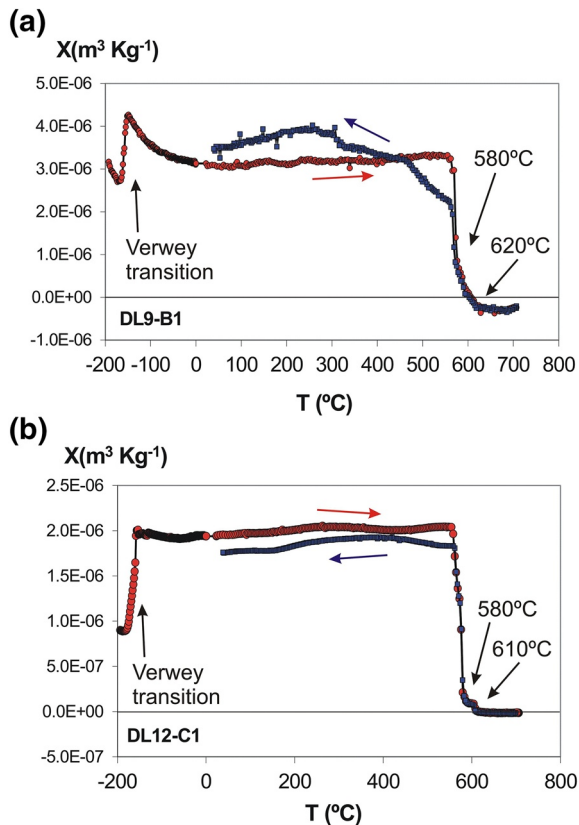
(a)

(b)

Figure 7. (a) Susceptibility thermomagnetic curves at low and high temperatures of samples DL9 (migmatite) and DL12 (inhomogeneous granite) showing a clear Verwey transition characteristic of magnetite. An important susceptibility decrease is observed at 580 °C, indicating also the presence of magnetite. A more subtle one exists at 610–620 °C, indicating the existence of low-Ti content Titanohematite. Both samples belong to Type (b).

Some standard samples have been thermally demagnetized after applying a composite three axis IRM, orthogonally induced at 2, 0.4, and 0.14 T, respectively (Lowrie, 1990). The IRM has been applied with a pulse magnetizer M2T-1 (Ferronato), the thermal demagnetization using a TD48-DC (ASC) thermal demagnetizer and the magnetization has been measured by means of a JR5 spinner magnetometer (AGICO). Results of this experiment are illustrated in Figure 9. The low coercivity fraction (<140 mT) presents unblocking temperatures between 100 and 300 °C, and more moderately around and above 500 °C, pointing to the existence of minerals of the titanomagnetite series, but mainly in a not-stable state as shown by these low unblocking temperatures. In addition, there is a remarkable medium-high coercivity fraction with drops at 620 and 670 °C indicating an important contribution of two phases of hematite or low-Ti hematite, coherent with the classification of these samples to the B-Type.

According to the above data, the ferromagnetic minerals observed on the rock magnetism experiments are dominated by two end-member behaviors: one with almost only Ti-free MD magnetite (Type A samples) and another one featuring magnetite with lesser amounts of Ti-low hematite (Type B samples).

3.3. Natural Remanent Magnetization (NRM)

A paleomagnetic study has been carried out on 39 paleomagnetic sites (ca. 200 cores) from the studied area. The natural remanent magnetization (NRM) has been measured using a 2G-755 cryogenic magnetometer at the Laboratory of Paleomagnetism of the Universidad de Burgos (Spain). The values of NRM are comprised between 0.1×10^{-3} A/m (DL-18) and 5 A/m (DL-26). However, most of the studied sites have a coherent and often strong NRM, showing an order of magnitude of 0.5 A/m. Table 1 and Figure 3b show the mean value of the NRM intensity for each paleomagnetic site, as well as the mean of susceptibility (κ). Parameter κ shows widespread values between 5×10^{-6} (SI) and 0.035 (SI) with a most common value ranging around 0.01 (SI). These values give rise to Königsberger ratios (Qn) that vary between 0.1 and 434, even though most samples have Qn values between 0.1 and 1. In Table 1 and Figure 3b, the parameters of NRM, the susceptibility and Qn are grouped by areas: Viveiró (in the center of the tectonic window, do not mistake with Viveiro, which lies in the coast ca. 20 km to the N), South Fault, East Ourol, Viveiro Fault, Rúa, North Fault, and Xove. Figure 3a includes color coded labels that allow to locate the high Qn samples in relation to the anomaly. Both parameters, NRM and κ, mostly show similar values for sites belonging to the same group, with the exception of (1) the East Ourol group that shows a heterogeneous behavior and (2) the very high Qn value sites, that belong to different groups (Figure 3b).

The NRM of all samples has been systematically demagnetized either thermally using a TD48-DC thermal demagnetizer or by alternating fields (AF) with a 2G magnetometer AF demagnetization unit. Figure 10 shows orthogonal and intensity decay plots of representative samples. In each example both thermal and AF demagnetizations of twin specimens are shown for comparison. The behavior of the NRM demagnetization can be grouped in three types.

Most samples can be assigned to Type 1 (Figures 10a and 10b) in which the NRM is composed of a single component with a high unblocking temperature spectrum between 580 and 680 °C. This component has high coercivity since it cannot be demagnetized applying AF with a peak field of 100 mT. This directional

Figure 6. Isothermal Remanent Magnetization (IRM) acquisition curves and backfield (left, (a) to (f)), induced magnetization thermomagnetic curves (center, g to l) and hysteresis loops (right, m to r) for selected samples. These are divided in two groups featuring a different behavior that can be classified between two end-members: Type (a) presents low coercivity phases and Curie Temperatures (Tc) typical of magnetite. Type (b) presents the same magnetite phase coexisting with higher coercivity and higher Tc typical of hematite.
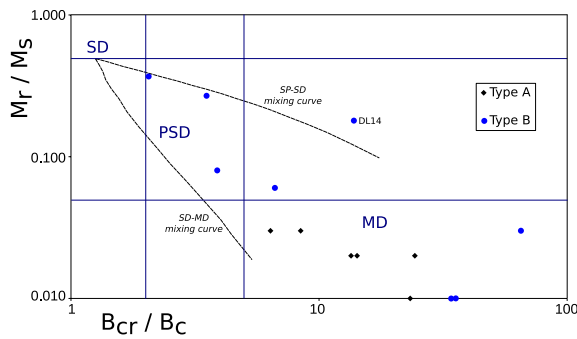
Figure 8. Day Plot of Type A (samples with mainly MD magnetite) and Type B (presence of a high coercivity and high Curie temperature ferromagnetic phase) samples. Theoretical curves (Dunlop, 2002) for SD-MD and SP-SD magnetite mixtures are also included. MD, multidomain.

component has been considered in this work as the characteristic remanent magnetization (ChRM) and is unequivocally carried by hematite, also in agreement with the results of the rock magnetic experiments. The diagrams of the decay of NRM during thermal demagnetization allow us to observe two inflections at 620 and 680 °C suggesting that two populations of hematite grains are responsible for the ChRM, with different grain size (e.g., compare hematite size in Figures 5b and 5f) or different degree of Ti substitutions.

In a second group of samples (Type 2) two components can be distinguished (Figures 10c and 10d). First a high unblocking temperature component with the same magnetic properties as the ChRM observed in the Type 1, e.g. unblocking temperatures >580 °C and high coercivity. In addition, a low coercivity component is also observed with variable maximum unblocking temperatures (350 °C in Figure 10c or 580 °C in Figure 10d). Based on the paleomagnetic direction, this low-temperature component can be clearly identified with the low coercivity fraction that can be isolated by the AF cleaning (Figures 10c and 10d). This component is probably due to titanomagnetite with different Ti content.

Finally, in some samples the high coercivity ChRM component is absent (Type 3). The complete NRM can be demagnetized by applying an AF with a peak field lower than 100 mT (Figures 10e and 10f). Accordingly, a unique low coercivity component exists and presents, as in Type 2, variable unblocking temperatures ranging between 350 and 580 °C (Figures 10e and 10f).

In summary, the NRM of most samples (Types 1 and 2) presents a very stable paleomagnetic component with consistent directions carried by two populations of hematite and which has been considered the ChRM in the subsequent interpretation. The site mean directions of this component have been plotted in Figure 11 and listed in Table 1. The ChRM component presents systematically reversed polarity (Figure 11a) and consistent directions in each area (Figure 11b). The mean declinations (D) vary from 132° to 202°, most of them around 160°. Inclinations (I) are usually low, generally from −18° to −41.5°, except to the N where they increase to about −60°. In Figure 11b, the most stable NRM directions (Table 1) are plotted in stereographic projection by groups and located in the magnetic map together with the position of the paleomagnetic Permian pole (270 Ma, Torsvik et al., 2012).

The low coercivity and low unblocking temperature components observed in groups Type 2 and 3 present directions with broadly normal polarity. However, they show widespread directions that do not allow a solid interpretation. As it will be discussed later, these scattered low coercivity components are probably viscous magnetizations carried by MD magnetite which has been observed in the rock magnetic experiments.
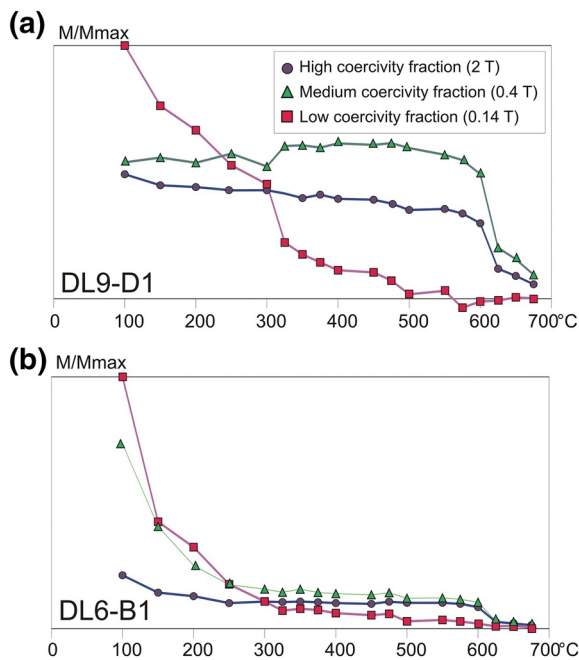
3.4. X-Ray Diffraction Analysis and Results

Mineralogical characterization of some samples (DL2-D, DL7-A, DL7-C, DL8-D, DL11-A, DL11-D, DL12-C, DL12-D, and DL13-E) was carried out by X-ray diffraction (XRD) using a SIEMENS D-500 diffractometer with Cu Kα and a graphite monochromator, at a scanning speed of 0.05°2θ/1s. The XRD studies were carried out in powdered samples (scanned from 2° to 65°2θ). In addition, a powdered concentrate of magnetic minerals extracted from DL8-D has also been studied. This sample has been labeled as DL8. In this case, the scanning speed was 0.05°2θ/3s to be able to obtain enough intensity of the peaks in a sample that is enriched in very radiation-absorbent minerals.

Figure 9. Thermal demagnetization of a composite three axis IRM (2 T, 0.4 T, and 0.14 T, respectively) over two representative samples (Type B DL9-D and DL6-B). Unblocking temperatures on the high and medium coercivity phase indicates the presence of hematite. Lower unblocking temperatures on the medium and low coercivity phase indicates the presence of magnetite.

Table 1
List of Paleomagnetic Sites Used in the Present Study.

Sites by groups	N	Lithology	ChRM Declination (°)	ChRM Inclination (°)	k	α_{95} (°)	NRM (A/m $\times 10^{-3}$)	k (S.I. $\times 10^{-3}$)	Qn
Viveiró									
DL11		Migmatite	–	–	–	–	3,000	6	12.5
DL36		Paragneiss	–	–	–	–	30	7	0.10714286
DL37	5	Granite	145.6	−41.5	196	6	300	35	0.21428571
DL38	8	Granite	150.8	−23.8	18	14	1,000	0.15	166.666667
DL39		Granite	–	–	–	–	20	5	0.1
South Fault									
DL04	3	Granite	184	−19	167	10	560		
DL10	2	Migmatite	171	−20	–	–	1,000	19	1.31578947
DL101	5	Migmatite	171	−21	37	13	1,500	10	3.75
DL29	6	Migmatite	152	−48	24	14	300	14	0.53571429
DL10 + DL101	7	Migmatite	167	−19	39	10			
East Ourol									
DL24		Granite	–	–	–	–	1	0.24	0.10416667
DL25	3	Quarcite	160	−29	69	15	600	6.5	2.30769231
DL26	5	Granite	164	−22	51	11	5,000	0.6	208.333333
DL27		Granite	–	–	–	–	20	2.4	0.20833333
DL28		Granite	–	–	–	–	0.3	0.003	2.5
Viveiro Fault									
DL18		Granite	–	–	–	–	0.1	0.015	0.16666667
DL23		Granite	–	–	–	–	0.08		
DL30	4	Quarcite	179	−70	94	9	200	0.005	1000
DL31		Quarcite	–	–	–	–	1	0.007	3.57142857
DL32		Quarcite	–	–	–	–	0.8	0.06	0.33333333
DL33	4	Schist	145	−18	9	33	0.3	0.09	0.08333333
DL34	4	Schist	150	−32	6	40	100	7	0.35714286
DL35	5	Paragneiss	139	−26	60	10	1,000	12	2.08333333
RÚA									
DL07	7	Granite	144	−49	49	9	130	10	0.325
DL12	4	Granite	189	−48	47	14	100	4.6	0.54347826
DL13	4	Granite	187	−62	689	4	300	13	0.57692308
DL16	4	Granite	164	−61	330	5	800	0.046	434.782609
DL19	5	Granite	143	−64	71	9	200	11	0.45454545
DL21		Paragneiss	–	–	–	–	0.5	0.07	0.17857143
DL22	2	Paragneiss	152	−51	260	8	150	7	0.53571429
North Fault									
DL15	6	Granite	134	−32	345	4	100	16	0.15625
DL17	7	Paragneiss	148	−26	49	9	70	5.8	0.30172414
Xove									
DL01		Granite	–	–	–	–			
DL02		Granite	–	–	–	–			

Table 1
Continued

Sites by groups	N	Lithology	ChRM Declination (º)	ChRM Inclination (º)	k	α_{95} (º)	NRM (A/m $\times 10^{-3}$)	k (S.I. $\times 10^{-3}$)	Qn
DL03	4	Granite	132	−61	17	23	700		
DL05	3	Granite	202	−76	16	32	80	4.8	0.41666667
DL06	2	Granite	168	−52	26	24	250	7.6	0.82236842
DL08	3	Granite	163	−59	47	18	200	13	0.38461538
DL09	3	Granite	142	−55	43	19	700	6.9	2.53623188
DL14	4	Granite	187	−70	74	11	400	9	1.11111111
DL20		Granite	–	–	–	–	4	0.8	0.125

Classification is geographical and based on those presenting strong NRM and homogeneous behavior. Mean site directions of the ChRM declination: (D), inclination (I), Fisher precision parameter (k) and confidence limit 95%. Site mean values of other magnetic parameters: magnetic susceptibility (κ) and Königsberger ratio (Qn). The lithologies are also specified for each sample. Granites are always inhomogeneous, i.e., syntectonic.
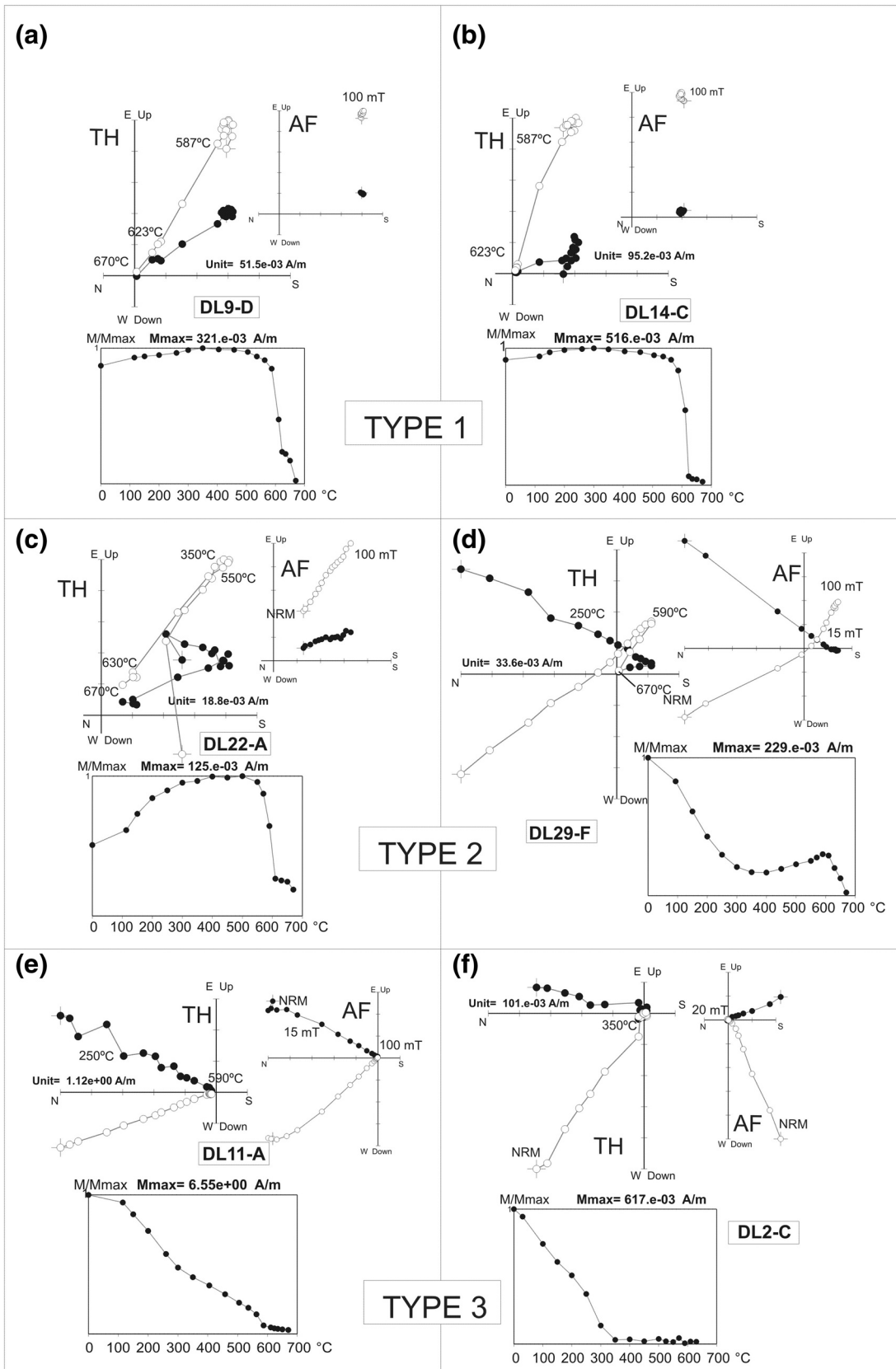
The mineralogical compositions of the raw samples are very similar. The main minerals are quartz and feldspars, and a minor proportion of micas can also be identified. There are small differences regarding feldspar content: Ca-plagioclase is the only feldspar in sample DL2-D. In the other samples, Ca-plagioclase appears together with K-feldspar but the plagioclase is more abundant in DL12-C, DL12-D, and DL13-E samples, while K-feldspar is more abundant in samples DL8-D and DL11-D. In the other three samples (DL7-A, DL7-C, and DL11-A) the proportion of Ca-plagioclase and K-feldspar is similar. As magnetic minerals are in low proportion and they are very absorbent of X-radiation, they cannot be identified in the raw powdered samples. However, after concentration of these minerals in DL8 sample different Fe-rich components can be identified. The XRD pattern of DL8 sample (Figure 12) shows mainly magnetite, in addition to hematite and ilmenite. A small proportion of remaining quartz, mica, and K-feldspar are also identified.

3.5. Anisotropy of the Magnetic Susceptibility (AMS)

In areas with heterogeneous deformation, the study of AMS helps to understand tectonics and, sometimes, the age and origin of magnetization. All 39 sites (about 200 samples) collected in the Xistral Tectonic Window have been analyzed using this technique. Samples include metasediments, syntectonic granites with varying degrees of deformation, post-tectonic granites and migmatites. Among samples, analyses have been made on leucosomes, melanosomes and fine and coarse-grained specimens. Results are presented in Figures 13 and 14.

None of the late Variscan granites (two sampled sites) provide coherent AMS results so they are excluded from the discussion. The rest of sites show ellipsoid orientations that are grouped by areas of coherent and similar anisotropy. To the W of the study area, samples are divided in four groups: VF1, VF2, VF3, and VF4. These groups include rocks that are in the western part of the Lugo Dome, where foliation is generally west-dipping, and were under the influence of the Viveiro shear zone. There, AMS results show a N-S to NNE-SSW planar magnetic foliation dipping to the W around 20–45°. These values are coincident with those of the structures associated to the Viveiro Fault, i.e., the SE2 schistosity and previous fabrics reoriented in its shear zone. To the SE of the study area, AMS results show a planar foliation striking ~ N40°E and dipping to the SE, in accordance with schistosity SE1 values found in the Viveiró area (group VO). Finally, in the NE part of the study area, an ill-defined AMS depicting a subhorizontal planar anisotropy reflects SE1 values in the hinge zone of the dome (groups NE1, and NE2).

In general, bulk susceptibility is very high, and is in agreement with that observed in the field, reaching κ = 0.054 (SI). Also, the anisotropy degree is anomalously high, getting to P = 2.405 in migmatite samples close to the Viveiro Fault (DL101, Figure 14). Relationships between bulk anisotropy (P) and shape of
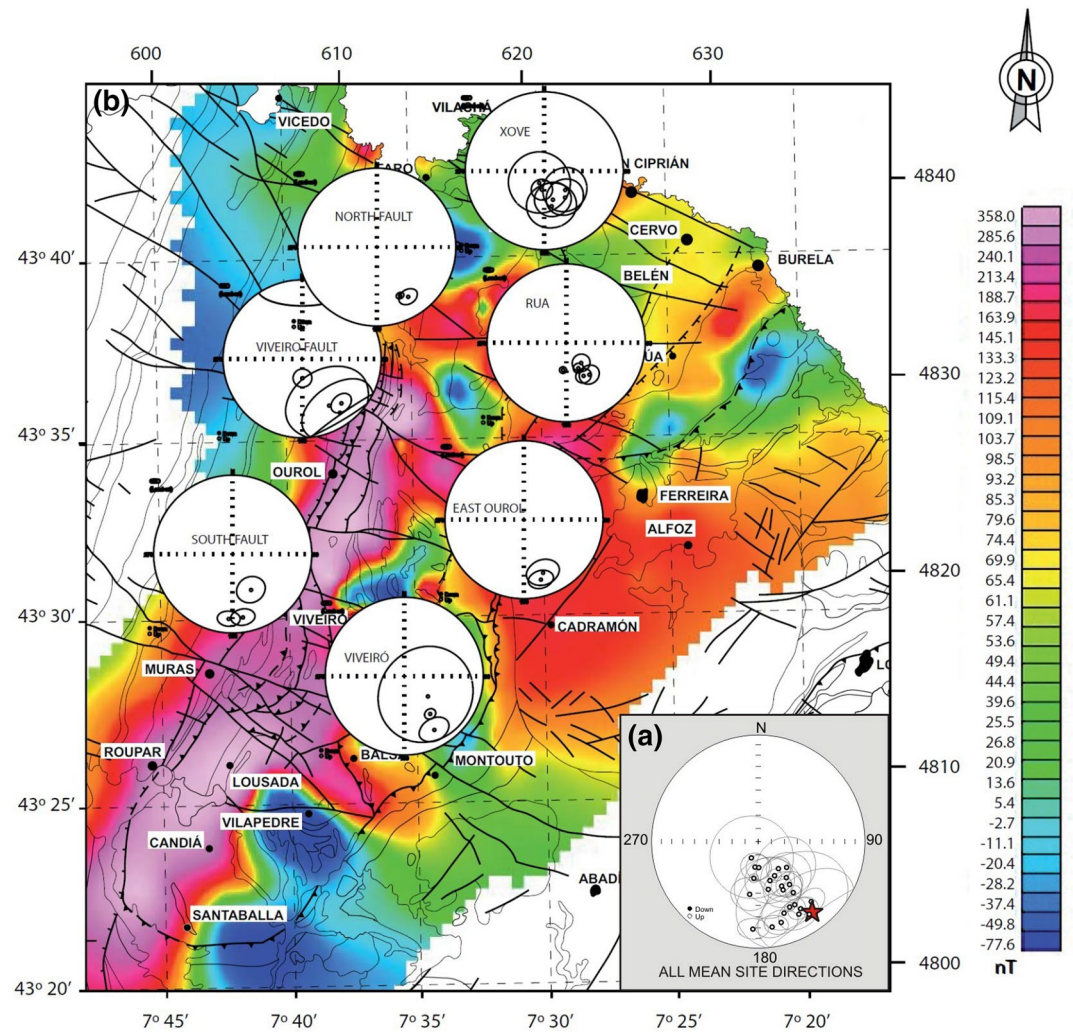
Figure 11. (a) Equal area projections showing the site mean directions of the ChRM component (see text) and the expected paleomagnetic direction for the Permian (red star) in NW Iberia coordinates (270 Ma, Dec = 143º, Inc = −20º, Torsvik et al., 2012). (b) Equal area projections of site mean directions grouped by regions and overlapping the absolute magnetic anomaly map of the Xistral Tectonic Window. Averages of mean site directions for each group are listed in Table 3. High inclinations shown for the Xove and Rúa Groups are probably the result of late or post-Variscan block tilting. ChRM, characteristic remanent magnetization.

the ellipsoid (T) and between P and mean magnetic susceptibility (κ_m) for different groups of samples are shown in Figure 14. The anisotropy ellipsoid is dominantly oblate in most samples, mainly in those near the Viveiro Fault (VF1, VF2, and VF3) with T usually positive and reaching 0.96. Also, a direct relationship has been observed between κ_m and P, pointing to the existence of magnetite as possible source of the anisotropy.

Figure 10. Orthogonal plots of NRM, alternating field (AF) and thermal demagnetization in geographical coordinates of three types of representative samples. Intensity decay plots for thermal demagnetization are also shown. Solid/open circles in orthogonal plots represent the projections of vector endpoints onto the horizontal/vertical and N-S planes. Type 1 is characterized by an unique high temperature/high coercivity component (ChRM) carried by hematite. Type 2 presents two components: a low coercivity/low-temperature component and the same high coercivity/higher temperature component of Type 1. Type 3 exhibits only an important low coercivity/low-temperature component being the hematite component observed in Types 1 and 2 absent. In each example both thermal and AF demagnetizations correspond to two twin specimens from the same core. NRM, natural remanent magnetization; ChRM, characteristic remanent magnetization.
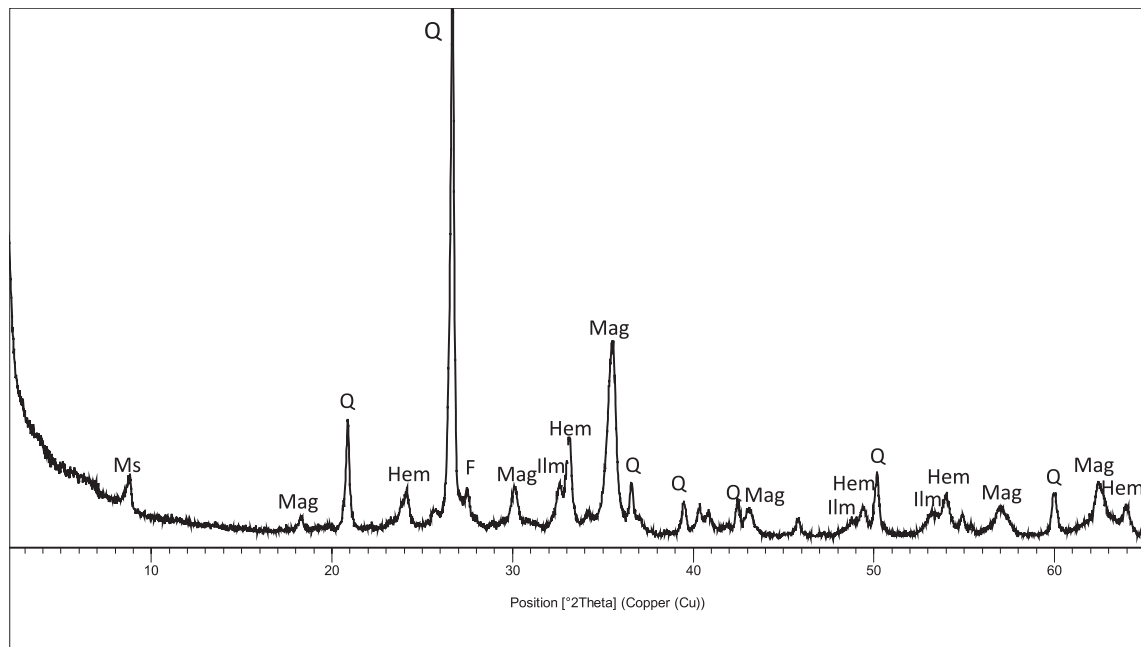
Figure 12. X-ray diffraction pattern of the magnetic fraction of sample DL8. Ms, muscovite; Mag, magnetite; Hem, hematite; Q, Quartz; Ilm, ilmenite.

3.6. Geochemical Characterization

Stable isotopes may be used to constrain the source material of granites and thus, to discern its character (e.g., Recio et al., 1992, and references therein). This is particularly interesting in the EGMA, where synkinematic igneous rocks appear to be heterogeneously magnetic whereas younger undeformed granites are not.

Oxygen and hydrogen isotope data have been determined for specific samples at the Servicio General de Análisis de Isótopos Estables (University of Salamanca, Spain). Oxygen isotope ratios were determined by laser fluorination (Clayton & Mayeda, 1963), employing a Synrad 25W CO_2 laser (Sharp, 1990) and ClF3 as reagent (e.g., Borthwick & Harmon, 1982). Isotope ratios were measured on a VG-Isotech SIRA-II dual-inlet mass spectrometer. D/H ratios were determined on a second SIRA-II mass spectrometer, on H_2 gas obtained by reduction over hot depleted-U of the water released by induction heating of samples. To this end, a vacuum line (Bigeleisen et al., 1952) was used, following the procedures described by Godfrey (1962), with modifications (Jenkin et al., 1992). Samples were loaded into degassed platinum crucibles that were placed into quartz reaction tubes and heated under vacuum to 125 °C overnight to remove any adsorbed H_2O. The yield of evolved gas was measured manometrically, and the value was used to determine the amount of structural water contained in the rock or mineral.

Internal and international reference standards (NBS-28, NBS-30) were run to check accuracy and precision. Results are reported in $\delta^{18}O$ and δD notation relative to the V-SMOW (Vienna Standard Mean Ocean Water) standard, using a $\delta^{18}O$ value of 9.6‰ for NBS-28 [quartz] and δD = −66.7‰ for NBS-30 [biotite] for the mass spectrometer calibration. Long-term reproducibility for repeated determination of reference samples was better than ±0.2‰ (1σ) for both $\delta^{18}O$ and δD.

$^{18}O/^{16}O$ ratios have been measured in 22 samples from 10 cores, two of them being early Cambrian schists, one magnetic (MCPG108, schists in Figures 2, 3, and 4c) and the other one not magnetic (MCPG85 in Figures 2 and 3). The rest of the samples are inhomogeneous granites and migmatites identified as highly magnetic (i.e., magnetite carriers) except for a weakly magnetic sample where hematite has been optically identified (DL26). In all cases analyses have been done in whole rock (WR) but in a few samples individual minerals have been analyzed too. Results are presented in Table 2.
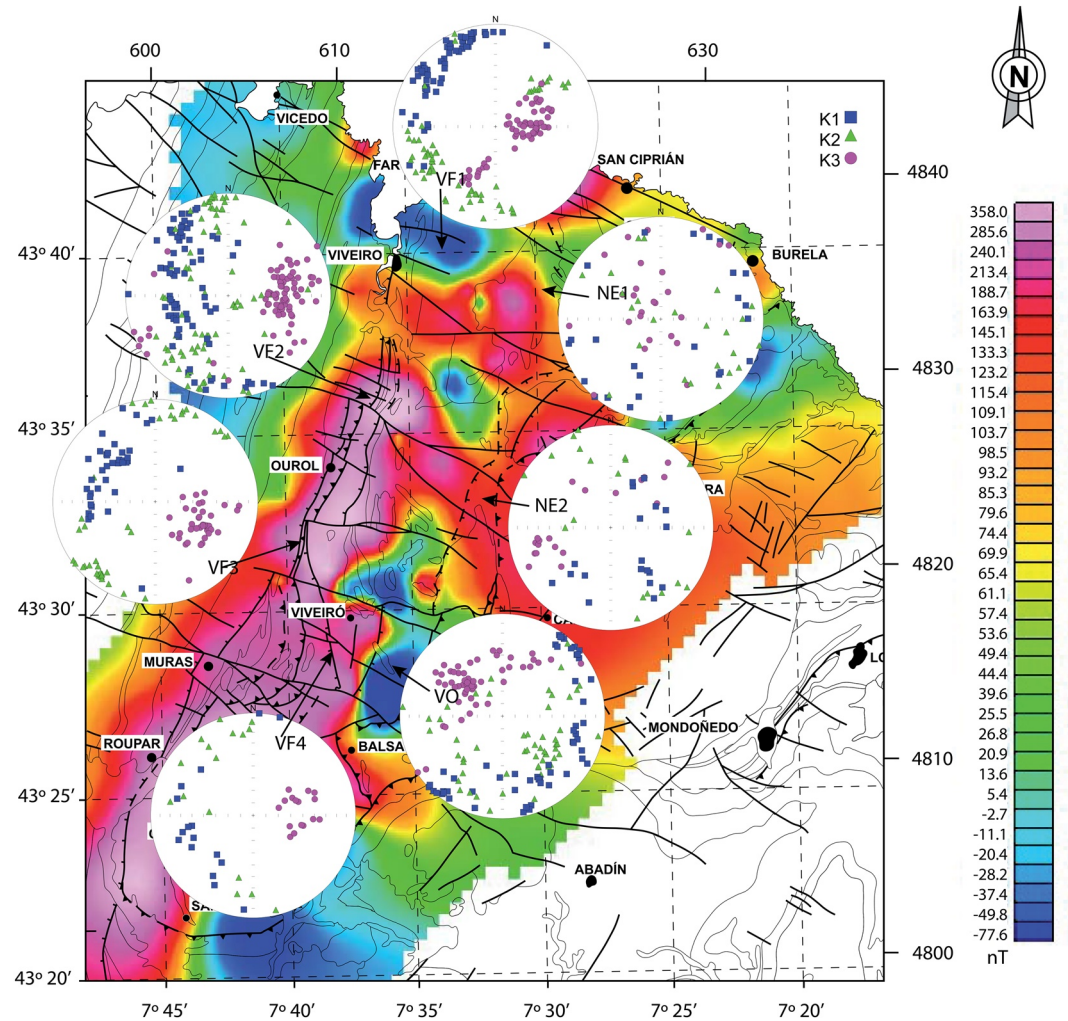
Figure 13. Equal area projection of in situ principal axis of the AMS grouped by similar behavior. VF1, VF2, VF3, and VF4 are located along the Viveiro Fault shear zone and show a planar magnetic anisotropy roughly parallel to the fault. VO represents a group close to the locality of Viveiró, where detachments show a low dip to the SE, as does the AMS. NE1 and NE2 are located to the NE of the study area. They show low AMS inclinations, coherent with a position close to the hinge zone of the Lugo Dome. Samples in each group are listed in Figure 14. Blue square: K1; Green triangle: K2: Purple circle: K3. Girdles defined by K1 and K2 indicate planar anisotropy whose attitude coincides with that of the main extensional detachments.

Values attained indicate that $\delta^{18}O$ is above 11.2‰ for inhomogeneous granites (WR), between 13.1‰ and 15‰ (WR) for migmatite samples, above 11.3‰ for nonmagnetic schists (WR and Ms) and 8.5–11.1‰ for magnetic ones. Magnetite from samples MCPG108 and DL8-D has $\delta^{18}O$ of 8.8‰ and 9.45‰ respectively. Hematite in DL26, the only sample where it could be isolated and measured, exhibits $\delta^{18}O = 11.2‰$. Biotite in this sample has high values of $\delta^{18}O$ reaching 12.1–12.5‰ as does muscovite, with $\delta^{18}O = 13.8$–13.9‰. Contrasting values are found for equivalent magnetic and nonmagnetic schists. The data suggest that the magnetization process undergone by these metasediments implies a marked decrease in $\delta^{18}O$ that affects all minerals and the whole rock (Table 2).

$\delta^{18}O$ values are very high in migmatites, indicating that they are derived from sediments. Inhomogeneous granites also feature high $^{18}O/^{16}O$ relationships indicating that they are S-Type granites (Chappell & White, 1974; Taylor & Sheppard, 2018). However, S-Type granites should belong to the Ilmenite-series (Ishihara, 1977), i.e., should be nonmagnetic. Contrarily, in the Xistral Tectonic Window these granites show, in places, high contents of magnetite, raising the question about its origin. Metasediments also show en-
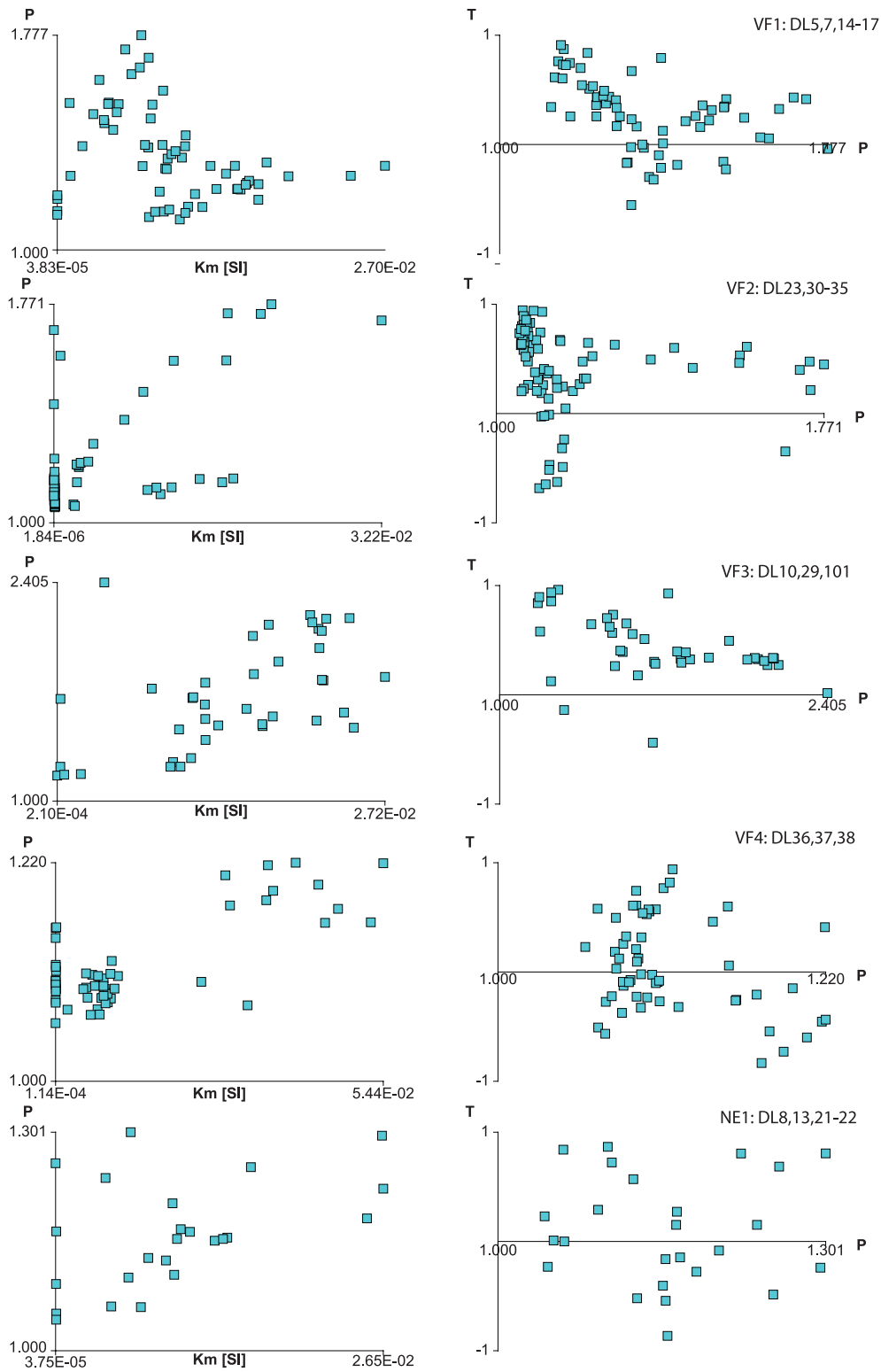
Figure 14. P-T diagrams for the more representative groups of samples studied by AMS. P, bulk anisotropy; T, shape of the ellipsoid; κ_m, magnetic susceptibility. Samples in each group are listed. AMS, Anisotropy of the Magnetic Susceptibility.

Table 2
Isotopic Oxygen Ratio ($^{18}O/^{16}O$) Expressed as $\delta^{18}O_{SMOW}$ in ‰

Sample	Phase	$\delta^{18}O_{VSMOW}$	Lithology
MCPG-108	Mag	8.8–9.1	Magnetic schist
MCPG-108	Bt	8.5–8.8	Magnetic schist
MCPG-108	Ms	11.1	Magnetic schist
MCPG-108	WR	10.5–11.1	Magnetic schist
DL26	Hem	11.2	Inhomogeneous granite
DL26	Bt	12.1–12.5	Inhomogeneous granite
DL26	Ms	13.8–13.9	Inhomogeneous granite
DL26	WR	13.6–13.7	Inhomogeneous granite
DL2-D	WR	11.6–11.7	Inhomogeneous granite
DL7-A	WR	12.5	Inhomogeneous granite
DL7-C5	WR	11.8–12.2	Inhomogeneous granite
DL8-D	Mag	9.3–9.4	Inhomogeneous granite
DL8-D	WR	11.8	Inhomogeneous granite
DL10	WR	13.1	Migmatite
DL11-A	WR	14.0	Migmatite
DL11-C	WR	15.0	Migmatite
DL11-D	WR	14.9	Migmatite
DL12	WR	11.7–12.1	Inhomogeneous granite
DL13	WR	11.5–11.8	Inhomogeneous granite
MCPG-85	Bt	11.3	Nonmagnetic schist
MCPG-85	Ms	13.7–13.9	Nonmagnetic schist
MCPG-85	WR	13.0–13.3	Nonmagnetic schist

Mag, Magnetite; Hem, Hematite; Bt, Biotite; Ms, Moscovite; WR, Whole rock. The column to the right specifies the lithology.

richment in the heavy oxygen isotope, as corresponds to rocks that have evolved in low-temperature conditions.

4. Interpretation of the EGMA

4.1. Origin of the EGMA: Induced Magnetization

Magnetic anomalies usually indicate the existence of rocks with high content of magnetite, the most magnetic mineral. However, NRM in igneous rocks is often triggered by hematite, which can have a stable single domain (SSD) behavior up to greater grain size than magnetite, further performing stable and strong remanence when being intergrowth with rutile (Robinson et al., 2002).

Optical and microprobe identification of magnetic minerals of our samples shows the existence of three types of magnetite and two types of hematite. Magnetite appears as regular crystals with ilmenite exsolutions (Figures 5a and 5c), altered to hematite (Figures 5b and 5c) and related to biotite, as a byproduct of its alteration or metamorphic evolution (Figure 5d). Hematite appears as result of the alteration of magnetite (Figures 5b and 5c) and as quite fresh crystals (Figure 5f), sometimes with exsolutions of rutile (Figure 5e).

Minerals presenting exsolutions seem to have an igneous origin, crystalizing slowly from a magmatic fluid. However, alteration of biotite to magnetite might be part of the metamorphic evolution of rocks prior to melting whereas that of magnetite to hematite could result from the interaction with an oxidizing agent. Further studies on the evolution of the magnetic minerals of these rocks are out of the scope of this paper. But the Fe-rich minerals relationships shown here seem to evidence a complex metamorphic evolution that led to a varied suite of magnetic minerals.

Rock magnetic studies have identified two end-member behaviors that allow us to classify the samples in two groups of magnetic rocks (Figure 6): A group (Type A) shows high amounts of mostly MD magnetite, whereas a second group (B-Type) exhibits a high coercivity fraction in ferromagnetic minerals (larger amounts of hematite) together with low coercivity fractions (lesser quantities of magnetite). IRM analyses show that samples identified as Type A need weaker magnetic fields to reach complete saturation (generally <200 mT), and show Tc = 576–587 °C, indicating that they are mostly magnetite bearing rocks. Contrarily, Type B samples need stronger magnetic fields (>300 mT) to reach saturation. These samples show Curie temperatures typical of magnetite (576-587 °C) in the thermomagnetic experiments, and a second drop at Tc = 580–620 °C that indicates the presence of Ti hematite.

Hysteresis loops (Figures 6g–6i) also allow us to classify samples in Types A and B. Type A cores includes the majority of samples, showing lower coercivity phases with characteristics compatible with MD magnetite (Figure 6). Contrarily, Type B features wasp-waisted curves (e.g., DL14 in Figure 6q) typical of mixtures of ferromagnetic grains with high and low coercivity compatible with the coexistence of magnetite and hematite as it has been observed in IRM studies. The contribution of paramagnetic minerals (biotite) in these samples, contrast with its scarce presence in Type A cores. This could be a manifestation of the metamorphic origin of magnetite after biotite, a process that might not affect hematite.

The Mrs/Mr and Bcr/Bc ratios as observed in a Day plot (Figure 8) suggest that most of the mentioned magnetite is in MD state, thus explaining the high values of κ in in situ and laboratory measurements. Thermomagnetic κT curves (Figure 7) acquired at low and high temperatures also confirm that high magnetic susceptibilities in these rocks are mostly the result of the amount of magnetite, although again, a small con-

Table 3
Average of Mean Site ChRM Directions Calculated by Groups (see Table 1)
for the Magnetic Remanence Measured in the Studied Samples of the
Xistral Tectonic Window

Group	N	D (°)	I (°)	K	α₉₅ (°)
Viveiró	3	148	−33	18	29
South Fault	3	169	−25	15	33
East Ourol	2	162	−26	–	–
Viveiro Fault	4	153	−37	10	30
Rúa	5	163	−56	51	11
North Fault	2	141	−29	–	–
Xove G	6	166	−63	33	12

Symbols as in Table 1.

tribution comes from low-Ti hematite. The identification of the Verwey transition, characteristic of pure magnetite further supports these results.

Last but not least, thermal demagnetization of a composite three axis IRM also shows the presence of low-Ti hematite in high and medium coercivity phases and magnetite and minerals of the titanomagnetite series in medium and low coercivity phases (Figure 9). Similar results are found by XRD (Figure 12) where magnetite and hematite appear to be the only magnetic minerals.

The demagnetization of the NRM shows, apparently, contrasting results to those obtained by rock magnetic analyses, and allow us to divide samples in three groups (Figure 10). Type 1 includes rocks where NRM responds solely to a unique directional component (ChRM) carried by hematite (maximum unblocking temperatures > 610 °C and no demagnetization at fields of up to 100 mT). In this case, Type 1 is by far the largest group. Among these samples (Figures 10a and 10b), most of them are classified as Type B in rock magnetic studies (e.g., DL9 and DL14; Figures 6e, 6f, 6k, 6r, 6q, and 6l), i.e., hematite-bearing rocks. Also, NRM studies identify a second group of samples, namely Type 2, featuring the coexistence of the hematite ChRM component and other component with low coercivity and intermediate unblocking temperatures typical of magnetite or titanomagnetite (e.g., DL22 and DL29 in Figures 10c and 10d) These samples are also classified as Type B. In a third group (Type 3) the NRM is dominated only by the mentioned low coercivity component carried by magnetite or titanomagnetite (e.g., DL11-A and DL2-C in Figures 10e and 10f) compatible with Type A rock magnetic behavior (Figures 6c, 6i, and 6o).

Both rock magnetic and NRM analyses show that magnetite and hematite are the main magnetic minerals in the rocks that are the source of the EGMA. However, results from both techniques apparently differ. Magnetite is the main mineral producing induced magnetization and the most outstanding in the first type of analyses whereas hematite is the responsible of most of the NRM and ChRM.

Nevertheless, the complete framework of paleomagnetic and rock magnetic analyses developed in this work is consistent with the interpretation of the coexistence of both populations of ferromagnétic s.l. minerals: (1) paleomagnetic stable hematite grains and (2) coarse-grained of magnetite in MD state. MD magnetite grains have a relatively low magnetic moment being less effective to contribute to the NRM. However, they have an extremely high induced magnetization enhancing the magnetic signal in susceptibility, hysteresis or thermomagnetic experiments. In addition, the high fields applied in the IRM experiments also enhance the contribution of MD magnetite grains, since the magnetic energy is enough to generate irreversible displacement of domain walls (Dunlop & Özdemir, 1997). All these effects can mask the signal of hematite which is undoubtedly present in most of these rocks as follows from the paleomagnetic results. Conversely, hematite, mostly when exsolved with rutile, is known to be an important contributor to remanence (Robinson et al., 2002). The wide variety of forms in which magnetite and hematite are found fosters the contrasting response of these magnetic rocks to different experiments. Finally, small differences in concentration of these two populations can explain the variability in rock magnetic experiments results between the end-members Type A and B, as well as in the NRM structure (Types 1, 2, and 3).

4.2. Characterization of the Natural Remanent Magnetization and its Contribution to the EGMA

Contrarily to what most authors have assumed in their magnetic models (e.g., Aller et al., 1994; Ayarza & Martínez Catalán, 2007; de Poulpiquet, 2012), the rocks that produce the EGMA feature a conspicuous remanence that has to be considered. Martínez Catalán et al. (2018) took into account preliminary results of the remanence studies presented here and included in the EGMA models a reverse polarity remanence of J = 0.267 A/m, D = 156°, and I = −28°. These data are an average of the measured values, although remanence is actually undersampled and very heterogeneous.

In the EGMA, the strongest NRM is carried by hematite (Type 1 in paleomagnetic studies, up to 1.5 A/m in DL101, 5 A/m in DL26, Table 1). Samples with very high Qn ratios have been identified (DL16, DL26, and DL38 in Table 1 and Figure 3b) and seem to be in relation with the location of inverse polarity parts of the EGMA (Figure 3a). But unfortunately, these types of rocks were not the goal of our surveying and were largely ignored, as in occasions, they performed very low κ values (κ = 0.0046–0.0006 (SI)) and were considered nonmagnetic. Accordingly, more detailed studies of remanence have to be carried out and probably different values of remanence need to be included in the models depending on the modeled sections.

Figure 3 shows that the high-resolution magnetic anomaly of the Xistral Tectonic Window systematically has minima to the SE of the maxima thus implying the existence of a strong remanence of reverse polarity. Figure 11 shows the equal area projection of mean site directions of the ChRM. D and I values are shown in Table 1 by groups and Table 3 presents the average for each group. Results are coherent for most samples, indicating that the observed inverse polarity supports a Kiaman reverse superchron remanent magnetization (Langereis & Krijgsman, 2008) when I is low, in agreement with the position of this part of Iberia at that time. However, to the N, the Rúa and the Xove groups show a remanence with similar D, but a considerably higher I, up to −62.5° (Table 3), somehow hindering this interpretation.

The Kiaman superchron embraces from the Pennsylvanian to the late Permian, more particularly between 318-312 and 262-251 Ma (Cottrell et al., 2008; Gradstein et al., 2004). The northern parts of the WALZ and the CIZ underwent compression from 360 to 305 Ma. Simultaneously, extension took place along two phases, E1 and E2, that covered a time span from 330 Ma to less than 300 Ma (Martínez Catalán et al., 2014). The Lugo-Sanabria Dome was going through a second stage of extension (E2) at 310-295 Ma, which implied generalized crustal melting and development of gneiss domes and extensional detachments at the beginning of the Kiaman superchron. Consistent D and I values observed in hematite-bearing samples carrying the ChRM in most of the Xistral Tectonic Window are coherent with a magnetization acquired during this reverse superchron. However, the mean inclination in most of the window, −28° (with southward declination), is high for a paleolatitude of ca. −6°S for this part of NW Iberia at 300 Ma (Pastor-Galán et al., 2016; Stampfli & Kozur, 2006; Weil et al., 2010; Stampfli & Kozur, 2006). A part of the inclination can be attributed to rotation during the opening of the Bay of Biscay during the Cretaceous. Higher inclinations close to the coast may result from complex block tilting of S dipping NW-SE faults defining a graben architecture in the northern part of the Lugo Dome, closer to the rift and where larger rotations can be expected.

Hematite is the mineral carrying the strongest ChRM reverse polarity. Figure 5 shows two types of hematite. The thermal demagnetization of NRM (Figures 10a–10c) and the rock magnetic studies (Figure 9a) also allows to distinguish between both types, showing maximum unblocking temperatures of 620 and 680 °C. One of these two types of hematite comes from the alteration of magnetite. The second type, unaltered and featuring exsolutions with rutile, seems to have a different origin. We suggest that during the first stage of extension (E1), MD magnetite crystallized. Ongoing extension implied an increase in the oxygen fugacity, producing more MD magnetite but mostly an alteration of magnetite to hematite and also the crystallization of new hematite. This latter process took place during E2, i.e., during the Kiaman superchron. Accordingly, MD magnetite developed during E1 is probably the most important contributor in the magnetic anomalies in the internal part of the CIA, thus picturing its curved geometry. Contrarily, E2 hematite is responsible for its remanence, which hinders the paleomagnetic investigations of pre-E2 events.

4.3. Structural Significance of the Magnetization

Magnetic lithologies in the Xistral Tectonic Window vary from schists and quartzites to migmatites and inhomogeneous granites. The structural analysis of these high-grade rocks is complex as their evolution is multiphase. One or more tectonic foliations exist in metasediments and in some synkinematic granitoids, but in most of the latter, including migmatites and inhomogeneous granitoids, the rocks appear to be undeformed although locally, traces of old foliations can be preserved. These are commonly discontinuous and often irregularly folded, and contrasting characteristics are often found between the leucosome and melanosome in diatexites and anatexites. Thus, AMS studies can help to unravel the deformation history of these high-T magnetic rocks.

AMS results (Figures 13 and 14) show that in the EGMA, AMS is very high. The direct relationship between AMS and κ (groups VF1-4, and NE1 in Figure 14) and the thermomagnetic κT curves (Figure 7) show that magnetite is the main carrier not only of the magnetic susceptibility but also of the magnetic anisotropy. The T parameter, also known as the shape factor (Jelinek, 1981) shows that this anisotropy is mostly planar close to the Viveiro Fault, and variably linear to planar to the E.

Figure 13 shows the AMS results overlapped to the high-resolution absolute magnetic anomaly of the Xistral Tectonics Window. The magnetic anisotropy mimics the foliation generated during the extensional stages, E1 and E2. It is particularly striking the high degree of anisotropy found to the W of the study area, which is in relation to the Viveiro Fault and its associated ductile extensional detachment, characterized by a strong SE2. Magnetic susceptibilities and the anomaly intensity are also higher in this area. Altogether, these data suggest that the Viveiro Fault, an E2 tectonic feature played a very important role in the development of the EGMA induced and remanent magnetization.

AMS results are less clear at the center and NE of the Xistral Tectonic Window but seem to be equally coherent with extensional deformation. In this area, two extensional detachments have been identified: the Lower Extensional Detachment and the Mondoñedo Nappe Basal Thrust, which was reactivated as an extensional detachment (Figure 2c). Both display a horizontal to shallow E-dipping fabric in the central and NE parts of the study area, where the VO, NE1 and NE2 groups were sampled. Accordingly, extensional detachments belonging to phases E1 and E2 seem to play again a decisive role in the origin of the magnetic anomalies.

In this regard, Martínez Catalán et al. (2018) already suggested that the origin of the EGMA was related with the extensional tectonics characteristic of the late stages of Variscan evolution in the present N Iberian Massif. These authors used the high-resolution map of the absolute magnetic anomaly of Figure 3 to carry out 2-D models showing that the anomaly could be mimicked by means of magnetic blocks parallel to extensional detachments, being the one associated to the Viveiro Fault the most important in terms of induced and remanent magnetization. This indicates that different rock types are magnetic when affected by an extensional detachment whereas they lack magnetic minerals when they are not, thus further supporting the key role of extensional tectonics in magnetization.

4.4. Geochemical Constraints on the Origin of Magnetization

Magnetic inhomogeneous granites and migmatites from the Xistral Tectonic Window present WR values of $\delta^{18}O = 11.5–15‰$ (Table 2). Enrichment in the heavier oxygen isotope shows that fractionation has occurred during low-temperature processes, such as subaerial weathering, and let us classify these granitoids as S-Type (Chappell & White, 1974; Taylor & Sheppard, 2018). According to Ishihara (1977), S-Type granitoids should belong to the ilmenite-series and ought to be nonmagnetic, as the high content in C-rich and S-rich minerals of the parent rock decreases oxygen fugacity thus leading to reduce conditions that prevent the formation of magnetite.

Classification of granites as Type-S and Type-I has been frequently challenged as some geochemical studies have shown that most granites, even those cited as typical examples of S-Type, show evidence for a mixture of mantle and upper crustal sources (Hopkinson et al., 2017 and references therein). However, it is clear that many of the granitoids of the Xistral Tectonic Window have a sedimentary/upper crustal source. Highly magnetic diatexites, where sedimentary layering can still be observed crop out parallel to the Viveiro Fault, and anatexites with abundant metasedimentary schlieren occur at the deep parts of the structure in the center of the window. Thus, it is striking to observe widespread development of magnetite in granitoids with such a clear sedimentary signature.

Several authors propose that occurrence of magnetite or ilmenite in granites is not only controlled by the oxygen fugacity of its source, but by magmatic differentiation and late magmatic processes (e.g., Pichavant et al., 1996; Villaseca et al., 2017). In fact, changes in the redox state of magmas have been attributed to interaction with external sources, like meteoric waters or the proximity to any other oxygen-rich atmosphere (Best, 2003). Magnetite bearing S-Type granites are scarce, but do exist. Some authors (e.g., Guo & Wilson, 2012) have describe magnetic S-Type granites in a context where metasomatic fluids and decompres-
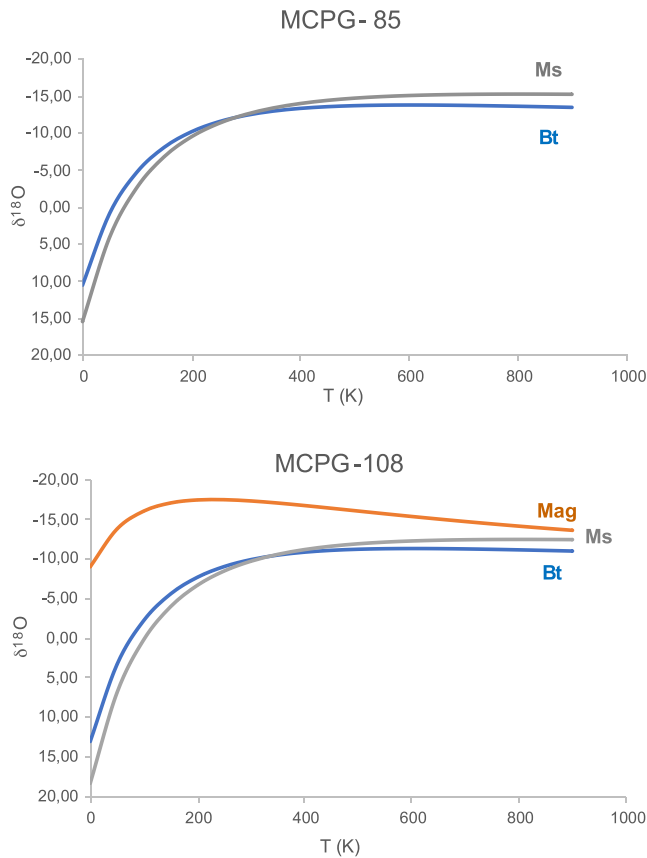
MCPG-85

MCPG-108

Figure 15. δ¹⁸O variation of water in equilibrium with magnetite (red curve), muscovite (yellow curve), and biotite (blue curve) calculated using the geothermometry equation $10^3 \ln\alpha_{(x\text{-}y)} = A10^6\, T^{-2} + B10^3\, T^{-1} + c)$ Constants are: Biotite: A = 3.840; B = −8.760; C = 2.460 (Zheng, 1993), Muscovite: (a) 4.100; (b) −7.610; (c) 2.250 (Zheng, 1993), Magnetite: (a) 3.020; (b) −12.000; (c) 3.310 (Zheng & Simon, 1991). Phases in equilibrium should result in curves crosscutting at the equilibrium temperature.

sion melting triggered by tectonics has played a key role in the change of the redox state of the magmas and the subsequent crystallization of magnetite.

Likewise, crustal melting in the NW of the Iberian Peninsula responds to the late stages of Variscan evolution, when crustal thickening led to melting, gravitational collapse and extension. Fluid circulation was probably significant along the extensional detachments, and probably contributed to change the redox conditions derived from the parent rock composition, leading to an increase in oxygen fugacity that controlled the crystallization of magnetite and hematite. This is supported by several facts observed in the study area: (1) magnetite occurrence in granitoids and metasediments is highly heterogeneous, ranging from nonmagnetic far from detachments to highly magnetic in the proximity of these structures; (2) AMS studies have demonstrated that magnetite developed a strong anisotropy parallel to the foliation in detachment zones; and (3) the high-resolution absolute magnetic anomaly of the Xistral Tectonic Window shows magnetic maxima along detachment zones, the most important of which occurs at the Viveiro Fault extensional shear zone.

Furthermore, δ¹⁸O values measured in muscovite, biotite, and magnetite (when present) for magnetic and not magnetic schists (MCPG108 and MCPG95; Table 2) have been plotted in an effort to see if they are in equilibrium and to constrain the temperature at which these phases crystallized. Constants needed for these calculations have been extracted from http://www2.ggl.ulaval.ca/cgi-bin/isotope/generisotope.cgi (Beaudoin & Therrien, 2009). Results, shown in Figure 15, demonstrate that muscovite and biotite are in equilibrium, being the T^a at which they have equilibrated the cross point of their respective curves (∼350 K). However, magnetite is not in equilibrium. As sample MCPG108 was collected in a detachment zone, probably the formation of magnetite was controlled by the entrance of an oxygen-rich source along this structure.

In order to constraint the characteristics of this O-rich source, values of δD have been measured for the same samples (Table 4) and WR values are plotted versus δ¹⁸O. Results are shown in Figure 16. The isotopic evolution from nonmagnetic to magnetic metasediments draws a straight line that points out toward the SMOW (Standard Mean Ocean Water) and/or low latitude meteoric waters, indicating that magnetization probably occurred as result of interaction with fluids of marine or meteoric affinity. These might have entered the system along detachment zones. The fact that magnetic schists became enriched in the light oxygen isotope thus decreasing its δ¹⁸O signature (see Table 2) implies that this process took place at relatively high temperatures (above 275 °C). The spatial heterogeneity found in the magnetization indicates that the entrance of fluids was not pervasive, but channelized along pathways inside the detachments.

4.5. Implications for the Origin of Other Magnetic Anomalies in the Central Iberian Arc

The Central Iberian Arc (CIA) was defined partly on the basis of the curvature delineated by magnetic anomalies in its internal part (Martínez Catalán, 2011). Most of these anomalies overlap thermal domes and accordingly, they might have an origin similar to the EGMA. The source of the other three outstanding anomalies (PVGMA, CSMA, and TDMA; Figure 1b) has not been thoroughly studied as yet. However, magnetic granites and/or magnetic high-grade metamorphic rocks are really scarce

Table 4
δD(SMOW) and % H₂O Content on Nonmagnetic (MCPG85) and Stratigraphically Equivalent (MCPG108) Schists

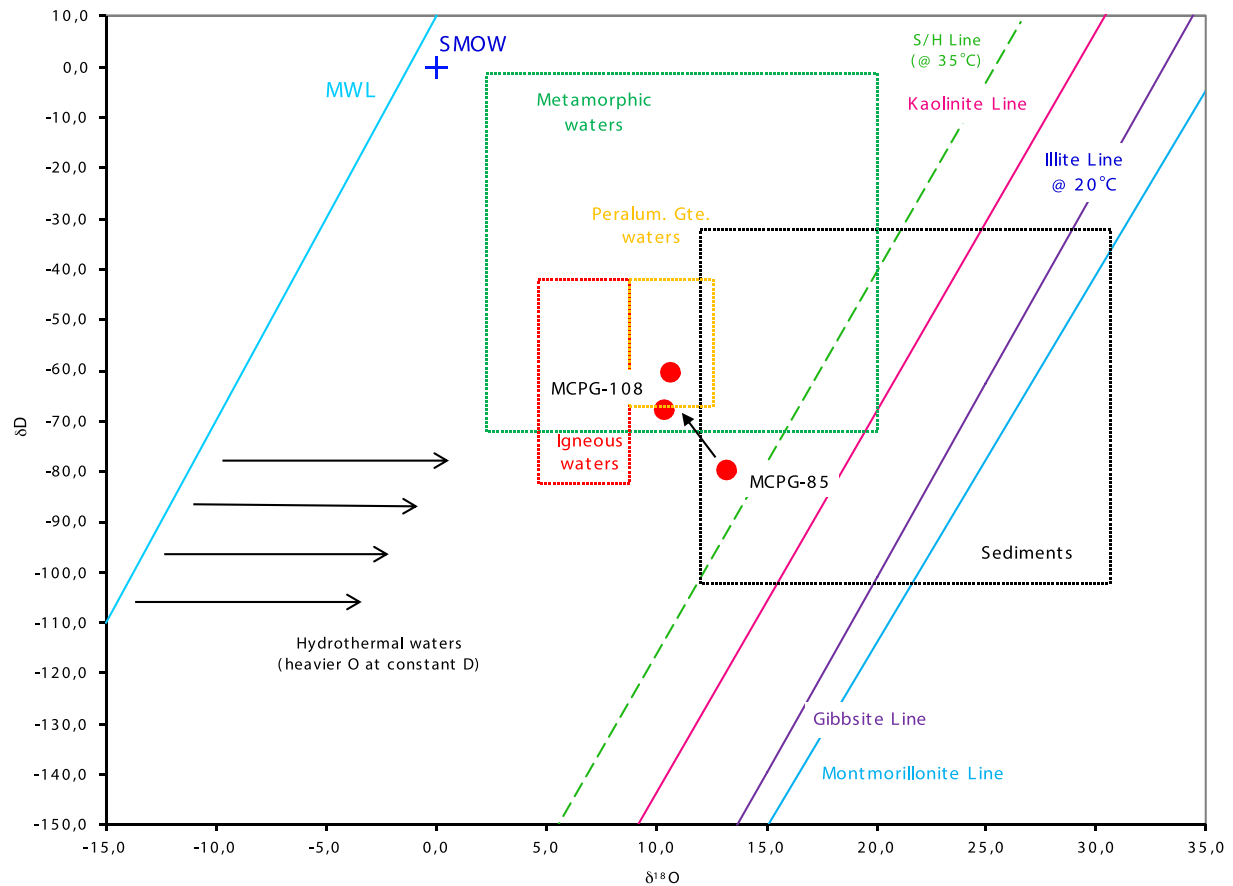| Sample	δD(SMOW)	% H₂O
MCPG85	−80.1	2.3
MCPG108	−60.4 to -67.9	3.3

Figure 16. Representation of δD y δ^{18}O values for whole rock (WR) in the context of the values for aqueous fluids of geological interest. MCPG85 is a nonmagnetic schist. MCPG108, is a stratigraphically equivalent magnetic schist outcropping at a detachment zone.

in these three areas. The PVGMA is the most extense of the four anomalies here considered. However, only the Lavadores granite, in the W part of the anomaly is significantly magnetic (Sant'Ovaia et al., 2013), providing little contribution to the anomaly itself, whose maximum is in the central part of northern Portugal. The CSMA is smaller and has less intensity than the PVGMA. Still, it is a conspicuous feature in the aeromagnetic map of the Iberian Peninsula, as it overlaps the Central System (Figure 1b), an area where Alpine tectonics has inverted Variscan faults (de Vicente et al., 2007; Vegas et al., 1990) exposing high-grade metasediments and orthogneisses, as well as late Variscan granitoids. However, the outcropping Central System lithologies are mostly nonmagnetic, and only some facies in La Pedriza batolith present moderate magnetic susceptibilities (Villaseca et al., 2017) that are largely insufficient to explain the anomaly. Lower crustal xenoliths and gabbros show higher magnetic susceptibilities but these do not abound, and likewise, cannot explain the anomaly either. Finally, the TDMA has been studied from a paleomagnetic point of view (Pastor-Galán et al., 2016) but magnetic susceptibility data has not been made available. However, preliminary surveying has demonstrated that the granitoids outcropping in this dome are not magnetic.

Portuguese Variscan granites and those of the Central System have been widely studied from a geochemical point of view (Martins et al., 2009; Recio et al., 1992; Villaseca et al., 1998). Even considering that the subdivision between S and I-Type depends on the tectonic context in which granites are formed and should not be taken as an absolute classification (Villaseca et al., 2017), granites in these areas seem to belong to both groups. But contrarily to what is observed in the Lugo Dome, the few magnetic granites identified in these locations (Lavadores in Portugal and La Pedriza in the Central System) belong to the I-Type.

These data reveal that in the CIA, magnetization is not associated with a particular type of granite, as considered from a geochemical point of view. But still, anomalies overlap thermal domes. We conclude that,

as in the EGMA, the DTMA, CSMA, and PVGMA might be controlled by tectonics and not so much by lithologies. Extensional detachments probably exist in all these thermal domes, buried at depth as in the Sanabria Dome or hidden by the massive intrusion of late-orogenic, undeformed granites. If these anomalies, all located in the NW Iberian Massif, also imply the existence of a Kiaman remagnetization, the age of the closure of the CIA or even its existence, cannot be established by paleomagnetic techniques alone (Pastor-Galán et al., 2020), as magnetic remanence is probably syn-to-post arc.

No tectonic window as that of Xistral exists or has been identified in the rest of the magnetic anomalies, thus hindering structural studies of deep rocks in those areas. One has to keep in mind that even though the source of the EGMA crops out in the Xistral Tectonic Window, the anomaly continues some 150 km to the S. Out of the tectonic window, no magnetic rocks have been found along the EGMA. Nevertheless, the fact that the anomaly continues and performs high amplitudes (Figure 1b) indicates that detachments still exist and deepen to the S as does the dome. The radially averaged power spectrum calculated from the aeromagnetic signature of the whole EGMA finds magnetic sources as deep as 12 km (Martínez Catalán et al., 2018), indicating that buried contributions to the anomaly do exist.

5. Conclusions

The Eastern Galicia Magnetic Anomaly (EGMA) is a natural laboratory to study the origin of aeromagnetic anomalies. The existence of the Xistral Tectonic Window, to the N of the Lugo-Sanabria Dome, onto which the EGMA overlaps, has allowed us to carry out detailed structural studies and a high-resolution surveying of this anomaly, as it provides large outcrops of its magnetic source rocks. These studies conclude that the EGMA features an important induced magnetization but also a conspicuous magnetic remanence that had not been deduced from the aeromagnetic map, but it is clearly identified when high-resolution ground magnetic data are obtained and source rocks are analyzed. Paleomagnetic analyses indicate that remanence, consistently of reverse polarity, was probably acquired during the Kiaman reverse superchron, simultaneously to late-orogenic melting and extension affecting the NW of the Iberian Massif. High inclinations found to the N of the anomaly might be due to Mesozoic block tilting of late Variscan faults.

The source of the induced magnetization seems to be mostly multidomain magnetite, which appears in three forms: in grains with exsolved ilmenite, in single crystals but altered to hematite and as result of alteration of biotite. The source of the remanent magnetization is mostly hematite, which appears in two contexts: as a byproduct of the alteration of magnetite and exsolved with rutile.

Anisotropy of the Magnetic Susceptibility Studies, detailed ground magnetic mapping and geochemical results indicate that magnetization (induced and NRM) was produced in metasediments, migmatites and inhomogeneous granites derived from them, only when affected by extensional detachments. As magnetic inhomogeneous granites belong to the S-Type, i.e., supposedly the nonmagnetic type, we suggest that the evolution of the magma in an extensional context modified the redox conditions of the melt, increasing the oxygen fugacity and allowing the crystallization of magnetite and even hematite. Stable isotopes results indicate that fluids of meteoric or marine affinity might have entered the system along these detachment zones and fostered the magnetization of the rock.

A similar origin is proposed for the rest of the magnetic anomalies found in the internal part of the Central Iberian Arc. These also overlap thermal domes but contrarily to the EGMA, no outcropping magnetic rocks have been identified so far. We propose that detachments developed during extension and melting exist at depth, as they probably do at the EGMA along the southern part of the Lugo-Sanabria Dome, and these are the source of the magnetic anomalies. A similar late Carboniferous-Permian (Kiaman) remagnetization might also exist thus erasing previous paleomagnetic indicators.

This interpretation might be key to understand worldwide magnetic anomalies located in extensional tectonic contexts. In addition, our work implies a warning on the complexity inherent to the understanding of aeromagnetic anomalies. Construction of reliable models needs to be aided by detailed ground surveying (magnetic and structural), paleomagnetic studies and petrological constraints. This paper represents an additional step on the knowledge of the EGMA and the other magnetic anomalies of the Central Iberian Arc and manifests the important role that extensional tectonics may play in mineralization.

Data Availability Statement

Ground-based magnetic data shown in this paper is available at Martínez Catalán et al. (2018). The reviews of Prof. Eric Font and Dr. Daniel Pastor Galán have helped to significantly improve this paper and thus, they are kindly thanked. This paper is dedicated to Fernando Alvarez-Lobato, who left us much too soon. He was a great colleague and an even better friend.

References

Aerden, D. G. A. M. (2004). Correlating deformation in Variscan NW-Iberia using porphyroblasts; implications for the Ibero-Armorican Arc. *Journal of Structural Geology*, *26*(1), 177–196. https://doi.org/10.1016/S0191-8141(03)00070-1

Alcock, J. E., Martínez Catalán, J. R., Rubio Pascual, F. J., Díez Montes, A., Díez Fernández, R., Gómez Barreiro, J., et al. (2015). 2-D thermal modeling of HT-LP metamorphism in NW and Central Iberia: Implications for Variscan magmatism, rheology of the lithosphere and orogenic evolution. *Tectonophysics*, *657*, 21–37. https://doi.org/10.1016/j.tecto.2015.05.022

Ali, M. Y., Fairhead, J. D., Green, C. M., & Noufal, A. (2017). Basement structure of the United Arab Emirates derived from an analysis of regional gravity and aeromagnetic database. *Tectonophysics*, *712–713*, 503–522. https://doi.org/10.1016/j.tecto.2017.06.006

Aller, J., Zeyen, H. J., Pérez-Estaún, A., Pulgar, J. A., & Parés, J. M. (1994). A 2.5D interpretation of the eastern Galicia magnetic anomaly (northwestern Spain): Geodynamical implications. *Tectonophysics*, *237*(3–4), 201–213. https://doi.org/10.1016/0040-1951(94)90255-0

Andrés, J., Marzán, I., Ayarza, P., Martí, D., Palomeras, I., Torné, M., et al. (2018). Curie Point Depth of the Iberian Peninsula and Surrounding Margins. *Journal of Geophysical Research*, *123*(3), 2049–2068.

Aranguren, A., Cuevas, J., Tubía, J. M., Román-Berdiel, T., Casas-Sainz, A., & Casas-Ponsati, A. (2003). Granite laccolith emplacement in the Iberian Arc: AMS and gravity study of the La Tojiza pluton (NW Spain). *Journal of the Geological Society*, *160*(3), 435–445. https://doi.org/10.1144/0016-764902-079

Aranguren, A., Garcia, C., & Tubia, J. M. (1991). *Estructura magnética de los macizos graníticos de Guitiriz y Hombreiro-Santa Eulalia de Pena (Lugo)*. Madrid, Spain: Sociedad Geológica de España.

Aranguren, A., & Tubia, J. M. (1994). Características estructurales y modelo de emplazamiento del plutón de Guitiriz (Galicia). *Revista de La Sociedad Geológica de España, 7*(1–2), 63–73.

Ardizone, J., Mezcua, J., & Socias, I. (1989). *Mapa aeromagnético de España peninsular, escala 1:1000000*. Madrid, Spain: Instituto Geográfico Nacional.

Arenas, R., & Martínez Catalán, J. R. (2003). Low-P metamorphism following a Barrovian-type evolution. Complex tectonic controls for a common transition, as deduced in the Mondoñedo thrust sheet (NW Iberian Massif). *Tectonophysics*, *365*(1–4), 143–164. https://doi.org/10.1016/S0040-1951(03)00020-9

Ayarza, P., & Martínez Catalán, J. R. (2007). Potential field constraints on the deep structure of the Lugo gneiss dome (NW Spain). *Tectonophysics*, *439*(1–4), 67–87.

Baptiste, J., Martelet, G., Faure, M., Beccaletto, L., Reninger, P. A., Perrin, J., & Chen, Y. (2016). Mapping of a buried basement combining aeromagnetic, gravity and petrophysical data: The substratum of southwest Paris Basin, France. *Tectonophysics*, *683*, 333–348. https://doi.org/10.1016/j.tecto.2016.05.049

Bascou, J. Ô., Henry, B., Ménot, R. P., Funaki, M., & Barruol, G. (2013). Contribution of AMS measurements in understanding the migmatitic terrains of Pointe Géologie, Terre Adélie (East-Antarctica). *Tectonophysics*, *603*, 123–135. https://doi.org/10.1016/j.tecto.2013.05.021

Beaudoin, G., & Therrien, P. (2009). The Web stable isotope fractionation calculator. In P. A. De Groot (Ed.), Handbook of stable isotope Analytical techniques, (Vol. II, pp. 1045–1047). Amsterdam: Elsevier. https://doi.org/10.1016/b978-044451114-0/50051-x

Best, M. G. (2003). *Igneous and metamorphic Petrology*. Malden, MA: Blackwell Publishing.

Bigeleisen, J., Perlman, M. L., & Prosser, H. C. (1952). Conversion of hydrogenic materials to hydrogen for isotopic analysis. *Analytical Chemistry*, *24*(8), 1356–1357. https://doi.org/10.1021/ac60068a025

Borthwick, J., & Harmon, R. S. (1982). A note regarding ClF3 as an alternative to BrF5 for oxygen isotope analysis. *Geochimica et Cosmochimica Acta*, *46*(9), 1665–1668. https://doi.org/10.1016/0016-7037(82)90321-0

Calvín, P., Casas, A. M., Villalaín, J. J., & Tierz, P. (2014). Reverse magnetic anomaly controlled by Permian igneous rocks in the Iberian Chain (N Spain). *Geológica Acta*, *12*(3), 193–207. https://doi.org/10.1344/GeologicaActa2014.12.3.2

Chappell, B. W., & White, A. J. R. (1974). Two contrasting granite types. *Pacific Geology*, *8*, 173–174.

Clayton, R. N., & Mayeda, T. K. (1963). The use of bromine pentafluoride in the extraction of oxygen from oxides and silicates for isotopic analysis. *Geochimica et Cosmochimica Acta*, *27*(1), 43–52. https://doi.org/10.1016/0016-7037(63)90071-1

Córdoba, D., Banda, E., & Ansorge, J. (1987). The Hercynian crust in northwestern Spain: A seismic survey. *Tectonophysics*, *132*(4), 321–333. https://doi.org/10.1016/0040-1951(87)90351-9

Cottrell, R. D., Tarduno, J. A., & Roberts, J. (2008). The Kiaman Reversed Polarity Superchron at Kiama: Toward a field strength estimate based on single silicate crystals. *Physics of the Earth and Planetary Interiors*, *169*(1–4), 49–58. https://doi.org/10.1016/j.pepi.2008.07.041

Dallmeyer, R. D., Martínez Catalán, J. R., Arenas, R., Gil Ibarguchi, J. I., Gutiérrez-Alonso, G., Farias, P., et al. (1997). Diachronous Variscan tectonothermal activity in the NW Iberian Massif: Evidence from 40Ar/39Ar dating of regional fabrics. *Tectonophysics*, *277*(4), 307–337. https://doi.org/10.1016/S0040-1951(97)00035-8

Day, R., Fuller, M., & Schmidt, V. A. (1977). Hysteresis properties of titanomagnetites: Grain-size and compositional dependence. *Physics of the Earth and Planetary Interiors*, *13*(4), 260–267.

de Poulpiquet, J. (2012). L'arc magnétique ibéro-armoricain est-il la trace d'un rift avorté d'âge. *Trabajos de Geología*, *32*, 76–86.

de Vicente, G., Giner, J. L., Muñoz-Martí, A., González-Casado, J. M., & Lindo, R. (1996). Determination of present-day stress tensor and neotectonic interval in the Spanish Central System and Madrid Basin, central Spain. *Tectonophysics*, *266*(1–4), 405–424. https://doi.org/10.1016/S0040-1951(96)00200-4

de Vicente, G., Vegas, R., Muñoz Martín, A., Silva, P. G., Andriessen, P., Cloetingh, S., et al. (2007). Cenozoic thick-skinned deformation and topography evolution of the Spanish Central System. *Global and Planetary Change*, *58*(1–4), 335–381. https://doi.org/10.1016/j.gloplacha.2006.11.042

Díez Fernández, R., & Pereira, M. F. (2017). Strike-slip shear zones of the Iberian Massif: Are they coeval?. *Lithosphere*, *9*(5), 726–744. https://doi.org/10.1130/L648.1

Díez Montes, A., Martínez Catalán, J. R., & Bellido Mulas, F. (2010). Role of the Ollo de Sapo massive felsic volcanism of NW Iberia in the early Ordovician dynamics of northern Gondwana. *Gondwana Research*, *17*(2–3), 363–376. https://doi.org/10.1016/j.gr.2009.09.001

Dufréchou, G., Harris, L. B., Corriveau, L., & Antonoff, V. (2015). Regional and local controls on mineralization and pluton emplacement in the Bondy gneiss complex, Grenville Province, Canada interpreted from aeromagnetic and gravity data. *Journal of Applied Geophysics*, *116*, 192–105. https://doi.org/10.1016/j.jappgeo.2015.03.015

Dunlop, D. J. (2002). Theory and application of the Day plot (Mrs/Ms versus Hcr/Hc). 1. Theoretical curves and tests using titanomagnetite data. *Journal of Geophysical Research*, *107*(B3), B12S30. https://doi.org/10.1029/2001JB000486

Dunlop, D. J., & Özdemir, Ö. (1997). *Rock magnetism. Fundamentals and frontiers.* Cambridge, UK:Cambridge Unviersity Press. https://doi.org/10.1017/CBO9780511612794

Fernández-Suárez, J., Dunning, G. R., Jenner, G. A., & Gutiérrez-Alonso, G. (2000). Variscan collisional magmatism and deformation in NW Iberia: Constraints from U-Pb geochronology of granitoids. *Journal of the Geological Society*, *157*(3), 565–576. https://doi.org/10.1144/jgs.157.3.565

Godfrey, J. D. (1962). The deuterium content of hydrous minerals from the East-central Sierra Nevada and Yosemite National Park. *Geochimica et Cosmochimica Acta*, *26*(12), 1215–1245. https://doi.org/10.1016/0016-7037(62)90053-4

Grauch, V. J. S., Hudson, M. R., & Minor, S. A. (2001). Aeromagnetic expression of faults that offset basin fill, Albuquerque basin, New Mexico. *Geophysics*, *66*(3), 707. https://doi.org/10.1190/1.1444961

Guo, Z., & Wilson, M. (2012). The Himalayan leucogranites: Constraints on the nature of their crustal source region and geodynamic setting. *Gondwana Research*, *22*(2), 360–376. https://doi.org/10.1016/j.gr.2011.07.027

Gutiérrez-Alonso, G., Collins, A. S., Fernández-Suárez, J., Pastor-Galán, D., González-Clavijo, E., Jourdan, F., et al. (2015). Dating of lithospheric buckling: 40Ar/39Ar ages of syn-orocline strike-slip shear zones in northwestern Iberia. *Tectonophysics*, *643*, 44–54. https://doi.org/10.1016/j.tecto.2014.12.009

Hopkinson, T. N., Harris, N. B. W., Warren, C. J., Spencer, C. J., Roberts, N. M. W., Horstwood, M. S. A., et al. (2017). The identification and significance of pure sediment-derived granites. *Earth and Planetary Science Letters*, *467*, 57–63. https://doi.org/10.1016/j.epsl.2017.03.018

Iglesias Ponce de León, M., & Choukroune, P. (1980). Shear zones in the Iberian Arc. *Journal of Structural Geology*, *2*(1), 63–68.

Ishihara, S. (1977). The magnetite-series and ilmenite-series granitic rocks. *Mining Geology*, *27*(145), 293–305.

Jelinek, V. (1981). Characterization of the magnetic fabric of rocks. *Tectonophysics*, *79*(3–4), 63–67. https://doi.org/10.1016/0040-1951(81)90110-4

Jenkin, G. R. T., Fallick, A. E., & Leake, B. E. (1992). A stable isotope study of retrograde alteration in SW Connemara, Ireland. *Contributions to Mineralogy and Petrology*, *110*(2–3), 269–288. https://doi.org/10.1007/BF00310743

Langereis, C. G., & Krijgsman, W. (2008). Geomagnetic polarity timescale. In F. M. Gradstein, J. G. Ogg, M. Schmitz, & G. Ogg (Eds.), *Encyclopedia of ocean sciences* (2nd ed.). Oxford, UK: Elsevier. https://doi.org/10.1016/B978-012374473-9.00244-7

Lawal, T. O., & Nwankwo, L. I. (2017). Evaluation of the depth to the bottom of magnetic sources and heat flow from high resolution aeromagnetic (HRAM) data of part of Nigeria sector of Chad Basin. *Arabian Journal of Geosciences*, *10*(17), 1–12. https://doi.org/10.1007/s12517-017-3154-2

Lowrie, W. (1990). Identification of ferromagnetic minerals in a rock by coercivity and unblocking temperature properties. *Geophysical Research Letters*, *17*(2), 159–162.

Martínez Catalán, J. R. (2011). Are the oroclines of the Variscan belt related to late Variscan strike-slip tectonics?. *Terra Nova*, *23*(4), 241–247. https://doi.org/10.1111/j.1365-3121.2011.01005.x

Martínez Catalán, J. R. (2012). The Central Iberian arc, an orocline centered in the Iberian Massif and some implications for the Variscan belt. *International Journal of Earth Sciences*, *101*(5), 1299–1314. https://doi.org/10.1007/s00531-011-0715-6

Martínez Catalán, J. R., Aerden, D. G. A. M., & Carreras, J. (2015). The "Castilian bend" of Rudolf Staub (1926): Historical perspective of a forgotten orocline in central Iberia. *Swiss Journal of Geosciences*, *108*(2–3), 289–303. https://doi.org/10.1007/s00015-015-0202-3

Martínez Catalán, J. R., Arenas, R., & Díez Balda, M. A. (2003). Large extensional structures developed during emplacement of a crystalline thrust sheet: The Mondoñedo nappe (NW Spain). *Journal of Structural Geology*, *25*(11), 1815–1839. https://doi.org/10.1016/S0191-8141(03)00038-5

Martínez Catalán, J. R., Ayarza, P., Álvarez Lobato, F., Villalaín, J. J., Durán Oreja, M., Martín Paramio, M., & Rodríguez Gómez, S. (2018). Magnetic anomalies in extensional detachments: The Xistral tectonic window of the Lugo dome (NW Spain). *Tectonics*, *37*(11), 4261–4284 https://doi.org/10.1029/2017TC004887

Martínez Catalán, J. R., Rubio Pascual, F. J., Díez Montes, A., Díez Fernández, R., Gómez Barreiro, J., Dias da Silva, Í., et al. (2014). The late Variscan HT/LP metamorphic event in NW and central Iberia: Relationships to crustal thickening, extension, orocline development and crustal evolution. *Geological Society, London, Special Publications*, *405*(1), 225–247. https://doi.org/10.1144/SP405.1

Martins, H. C. B., Sant'Ovaia, H., & Noronha, F. (2009). Genesis and emplacement of felsic Variscan plutons within a deep crustal lineation, the Penacova-Régua-Verín fault: An integrated geophysics and geochemical study (NW Iberian Peninsula). *Lithos*, *111*(3–4), 142–155. https://doi.org/10.1016/j.lithos.2008.10.018

Merino-Tomé, O. A., Bahamonde, J. R., Colmenero, J. R., Heredia, N., Villa, E., & Farias, P. (2009). Emplacement of the Cuera and Picos de Europa imbricate system at the core of the Iberian-Armorican arc (Cantabrian zone, north Spain): New precisions concerning the timing of arc closure. *Bulletin of the Geological Society of America*, *121*(5–6), 729–751. https://doi.org/10.1130/B26366.1

Miranda, J. M., Galdeano, A., Rossignol, J. C., & Mendes Victor, L. A. (1989). Aeromagnetic anomalies in mainland Portugal and their tectonic implications. *Earth and Planetary Science Letters*, *95*(1–2), 161–172. https://doi.org/10.1016/0012-821X(89)90174-X

Palencia Ortas, A., Osete, M. L., Vegas, R., & Silva, P. (2006). Paleomagnetic study of the Messejana Plasencia dyke (Portugal and Spain): A lower Jurassic paleopole for the Iberian plate. *Tectonophysics*, *420*(3), 455–472. https://doi.org/10.1016/j.tecto.2006.04.003

Parga Pondal, I., Matte, P. H., & Capdevila, R. (1964). Introduction a la geologie de l'Ollo de Sapo Formation porphyroïde antesilurienne du nord ouest de l'Espagne. *Trabajos del Laboratorio Geológico de Laxe*, *18*, 119–154.

Pastor-Galán, D., Dekkers, M. J., Gutiérrez-Alonso, G., Brouwer, D., Groenewegen, T., Krijgsman, W., et al. (2016). Paleomagnetism of the Central Iberian curve's putative hinge: Too many oroclines in the Iberian Variscides. *Gondwana Research*, *39*, 96–113. https://doi.org/10.1016/j.gr.2016.06.016

Pastor-Galán, D., Gutierrez-Alonso, G., & Weil, A. B. (2020). The enigmatic curvature of Central Iberia and its puzzling kinematics. *Solid Earth*, *11*(4), 1247–1273. https://doi.org/10.5194/se-11-1247-2020

Pedreira, D., Pulgar, J. A., Gallart, J., & Torné, M. (2007). Three-dimensional gravity and magnetic modeling of crustal indentation and wedging in the western Pyrenees-Cantabrian Mountains. *Journal of Geophysical Research: Solid Earth*, *112*(12), 1–19. https://doi.org/10.1029/2007JB005021

Pérez-Estaún, A., Martínez Catalán, J. R., & Bastida, F. (1991). Crustal thickening and deformation sequence in the footwall to the suture of the Variscan belt of northwest Spain. *Tectonophysics*, *191*(3–4), 243–253. https://doi.org/10.1016/0040-1951(91)90060-6

Pichavant, M., Hammouda, T., & Scaillet, B. (1996). Control of redox state and Sr isotopic composition of granitic magmas: A critical evaluation of the role of source rocks. *Earth and Environmental Science Transactions of the Royal Society of Edinburgh*, *87*(1–2), 321–329. https://doi.org/10.1017/s0263593300006714

Recio, C., Fallick, A. E., & Ugidos, J. M. (1992). A stable isotopic (D-18O, D-D) study of the late-Hercynian granites and their Host-rocks in the central Iberian Massif (Spain). *Transactions of the Royal Society of Edinburgh Earth Sciences*, *83*, 247–257.

Robinson, P., Harrison, R. J., McEnroe, S. A., & Hargraves, R. B. (2002). Lamellar magnetism in the hematite-ilmenite series as an explanation for strong remanent magnetization. *Nature*, *418*(6897), 517–520. https://doi.org/10.1038/nature00942

Salem, A., Green, C., Ravat, D., Singh, K. H., East, P., Fairhead, J. D., et al. (2014). Depth to Curie temperature across the central Red Sea from magnetic data using the de-fractal method. *Tectonophysics*, *624–625*, 75–86. https://doi.org/10.1016/j.tecto.2014.04.027

Sant'Ovaia, H., Martins, H., & Noronha, F. (2013). Oxidized and reduced Portuguese Variscan granites associated with W and Sn hydrothermal lode deposits: Magnetic susceptibility results (Granitos Variscos portugueses oxidados e reduzidos e sua associação com mineralizações hidrotermais de W e Sn : resulta). *Comunicações Geológicas*, *100*(1), 33–39.

Sharp, Z. D. (1990). A laser-based microanalytical method for the in situ determination of oxygen isotope ratios of silicates and oxides. *Geochimica et Cosmochimica Acta*, *54*(5), 1353–1357. https://doi.org/10.1016/0016-7037(90)90160-M

Socias, I., & Mezcua, J. (2002). *Mapa de Anomalias Magnéticas de la Peninsula Ibérica*. Madrid, Spain: Instituo Geográfico Nacional.

Stampfli, G. M., & Kozur, H. W. (2006). Europe from the Variscan to the Alpine cycles. *Geological Society Memoir*, *32*, 57–82. https://doi.org/10.1144/GSL.MEM.2006.032.01.04

Taylor, H. P., Jr., & Sheppard, S. M. F. (2018). Chapter 8. Igneous Rocks: I. Processes of isotopic fractionation and isotope systematics. In J. W. Valley, H. P. Taylor, & J. R. O'Neil (Eds.), *Stable isotopes in high temperature geological processes* (pp. 227–272). Berlin: De Gruyter. https://doi.org/10.1515/9781501508936-013

Torsvik, T. H., Van der Voo, R., Preeden, U., Mac Niocaill, C., Steinberger, B., Doubrovine, P. V., et al. (2012). Phanerozoic polar Wander, Paleogeography and dynamics. *Earth-Science Reviews*, *114*(3–4), 325–368. https://doi.org/10.1016/j.earscirev.2012.06.007

Vegas, R., Vázquez, J. T., Suriñach, E., & Marcos, A. (1990). Model of distributed deformation, block rotations and crustal thickening for the formation of the Spanish Central System. *Tectonophysics*, *184*(3–4), 367–378. https://doi.org/10.1016/0040-1951(90)90449-I

Verwey, E. J. W. (1939). Electronic Conduction of magnetite (Fe3O4) and its transition point at low temperatures. *Nature*, *144*, 327–328.

Villaseca, C., Barbero, L., & Rogers, G. (1998). Crustal origin of Hercynian peraluminious granitic batholiths of Central Spain: Petrological, geochemical and isotopic (Sr, Nd) constraints. *Lithos*, *43*, 55–79.

Villaseca, C., Ruiz-Martínez, V. C., & Pérez-Soba, C. (2017). Magnetic susceptibility of Variscan granite-types of the Spanish central system and the redox state of magma. *Geológica Acta*, *15*(4), 379–394. https://doi.org/10.1344/GeologicaActa2017.15.4.8

Walz, F. (2002). The Verwey transition - a topical review. *Journal of Physics: Condensed Matter*, *14*(12), 285–340. https://doi.org/10.1088/0953-8984/14/12/203

Weil, A., Gutiérrez-Alonso, G., & Conan, J. (2010). New time constraints on lithospheric-scale oroclinal bending of the Ibero-Armorican Arc: A paleomagnetic study of earliest Permian rocks from Iberia. *Journal of the Geological Society*, *167*(1), 127–143. https://doi.org/10.1144/0016-76492009-002

Zheng, Y.-F. (1993). Calculation of oxygen isotope fractionation in hydroxyl-bearing silicates. *Earth and Planetary Science Letters*, *120*, 247–263. Retrieved from https://ac.els-cdn.com/0012821X93902433/1-s2.0-0012821X93902433-main.pdf?_tid=094fc98f-d14e-479a-b4b1-cd-4b212e5f7f&acdnat=1549975407_d1e0c3d3f50928185edf5bb7f282afc0 http://www.geosc.psu.edu/Courses/Geosc518/4_Sample_Prep/Cha–pter_4/4_5_Oxygen/4_5_3_Sili

Zheng, Y.-F., & Simon, K. (1991). Oxygen isotope fractionation in hematite and magnetite: A theoretical calculation and application to geothermometry of metamorphic iron-formations. *European Journal of Mineralogy*, *3*(5), 877–886. https://doi.org/10.1127/ejm/3/5/0877